POLITECNICO DI MILANO
School of Industrial and Information Engineering
Department of Aerospace Science and Technology
Master of Science in Space Engineering


# Optimisation of kinetic impactor trajectory through guidance navigation and control during asteroid approach phase

**Advisor:** Prof. Pierluigi Di Lizia
**Co-Advisor:** Prof. Camilla Colombo

**Master thesis by:**
Claudio Faggioni
ID 883789

**Academic Year 2019-2020**

Printed in Italy

# Ringraziamenti

Prima di tutto vorrei ringraziare i miei relatori, Pierluigi Di Lizia e Camilla Colombo, per avermi dato l'opportunità di lavorare su questo interessante ed attuale argomento ingegneristico/scientifico. Sono grato della vostra constante disponibilità e dei giusti consigli che mi avete dato per risolvere i problemi che mano a mano si presentavano nello sviluppo del lavoro.

Poi vorrei ringraziare la mia famiglia, a partire dai miei genitori Dario e Gabriella, per il loro sostegno morale e per avermi dato la possibilità di frequentare il Politecnico di Milano. Vorrei ringraziare anche le mie sorelle Sara e Lucia con i rispettivi mariti Luca e Alessadro, per aver allietato con la loro presenza tutti i fine settimana. Ovviamente, un grande ringraziamento va a mia nipote Silvia che nell'ultimo anno ha sempre portato felicità nei miei pomeriggi.

Poi vorrei ringraziare tutti i miei colleghi del politecnico: Daniele, Emanuele, Federico, Francesca, Franscesco, Laura, Lele, Luca, Marco, Margherita, Marzia, Matteo, Sebastiano, Stefano. Abbiamo affrontato tante difficoltà insieme ma ne siamo usciti tutti alla fine. Da voi ho imparato molto e avete reso questi anni speciali e indimenticabili.

Infine, per ultima ma non meno importante, vorrei ringraziare di cuore la mia ragazza, Giada. Ti ringrazio per avermi sempre sostenuto e avermi ispirato in questi anni di università; sei sempre stata un esempio di impegno per me. Ti ringrazio anche di avermi sopportato per tutti questi anni che tra poco si fanno fatica addirittura a contare su due mani, di avermi regalato tanto amore e di rendere la mia vita così perfetta. Sei la mia felicità.

Milano, June 2020 Claudio Faggioni

# Abstract

Asteroids are one of the most common celestial bodies that populate our solar system; some of them come close to Earth and are identified as Near Earth Objects (NEO). The effects that an impact of one of these objects could cause to Earth, have stimulated the scientific community to investigate possible solutions to avoid this threat.
One possible technology for asteroid deflection and the highest in technology readiness level is the kinetic impactor strategy: it consists of a spacecraft that is inserted in route of collision with a threatening asteroid and exploits very high relative velocities between spacecraft and NEO to impart a momentum to deviate the orbit of the target.
This thesis focuses on the development of a general tool to optimise the orbit of the impactor by including in the optimisation loop a simulation of the guidance and control that the spacecraft would perform in a real scenario. Moreover, this tool can deal with different dimensions, shapes and orbits of a target NEO.
During the optimisation, the guidance and control take advantage of synthetic images of the asteroid that are generated and processed to obtain realistic measurements. From the real time simulation of the approaching phase towards the asteroid, the impact point and the momentum variation achieved are computed; the momentum variation of the NEO obtained is compared with the theoretical one via a parameter of merit called efficiency of impact.
Without loss of generality, the developed tool is tested on the object 2010RF12, an asteroid currently in the risk list of the NEOs with the highest probability of impact with the Earth. Results show that the developed tool is capable of optimise the orbit of the spacecraft also including the simulation of the approach phase to the asteroid.

# Sommario

Gli asteroidi sono alcuni degli oggetti celesti più comuni che popolano il nostro sistema solare; alcuni di loro passano vicino alla Terra e sono identificati come Near Earth Objects (NEO). Gli effetti che un impatto con uno di questi oggetti potrebbe causare alle Terra, ha spinto la comunità scientifica a investigare le possibili soluzioni per evitare questo rischio.
Una possibile tecnologia per deviare asteroidi and quella già disponibile a livello tecnologico, è la strategia dell'impattatore cinetico; si tratta di una sonda spaziale che è inserita in rotta di collisione con l'asteroide e sfrutta una velocità relativa molto alta per impartire al bersaglio abbastanza momento per deviarne l'orbita.
Questa tesi si focalizza sullo sviluppo di uno strumento generale per ottimizzare l'orbita dell'impattatore includendo nel processo di ottimizzazione la simulazione della guida e del controllo che la sonda compierebbe in uno scenario reale. Inoltre, questo strumento può far fronte a diverse dimensioni, forme e orbite di un NEO bersaglio.
Durante l'ottimizzazione, il sistema di guida utilizza immagini sintetiche dell'asteroide che sono generate e processate per ottenere misure realistiche. Dalla simulazione in tempo reale della fase di approccio verso l'asteroide, vengono calcolati il punto di impatto e la variazione del momento dell'asteroide; essa viene poi confrontata con la variazione di momento teorica attraverso un parametro di merito chiamato efficienza dell'impatto.
Senza perdita di generalità, lo strumento sviluppato è testato sull'oggetto celeste 2010RF12, un asteroide attualmente prensente nella lista di rischio dei NEO che hanno la più alta probabilità di un impatto con la Terra. I risultati mostrano che lo strumento sviluppato è in grado di ottimizzare l'orbita della sonda spaziale includendo la simulazione della fase di approccio all'asteroide.

# Contents

# List of Figures

# List of Tables

# Acronyms

| Acronym | Definition |
|---|---|
| AIDA | Asteroid Impact and Deflection Assessment |
| ASI | Agenzia Spaziale Italiana |
| CNEOS | Center for Near-Earth Object Studies |
| CNES | Centre National d'Études Spatiales (national centre for space studies) |
| DART | Double Asteroid Redirection Test |
| DLR | Deutsches Zentrum für Luft-und Raumfahrt (German aerospace centre) |
| DSM | Deep Space Manoeuvre |
| ESA | European Space Agency |
| IAC | International Astronautical Congress |
| IAWN | International Asteroid Warning Network |
| JAXA | Japan Aerospace Exploration Agency |
| MOID | Minimum Orbital Intersection Distance |
| NASA | National Aeronautics and Space Administration |
| NEA | Near-Earth Asteroid |
| NEO | Near-Earth Object |
| NEOCC | Near-Earth Object Coordination centre |
| SMPAG | Space Mission Planning Advisory Group |
| TRL | Technology Readiness Level |

# Nomenclature

| Symbol | Unit | Definition |
|---|---|---|
| $Alb_{NEO}$ | [-] | NEO albedo |
| a | [km] | Orbit semi-major axis |
| $D_{NEO}$ | [m] | NEO mean diameter |
| e | [-] | Orbit eccentricity |
| FL | [mm] | Focal length |
| FOV | [deg] | Field of View |
| $g_0$ | [m/s$^2$] | Earth's surface gravity acceleration |
| Isp | [s] | Specific impulse |
| i | [rad] or [deg] | Orbit inclination |
| MOID | [km] | Minimum Orbit Intersection Distance |
| $P_{hit}$ | [-] | Probability of impact |
| Res | [px] | Resolution of the detector |
| $r_p$ | [km] | Radius of pericentre |
| $Sens_{size}$ | [mm] | Size of the detector |
| TOF | [days] | Time Of Flight |
| $t_{subscript}$ | [s] or [days] | Time at which subscript happens |
| $\mathbf{v}$ | [km/s] | Spacecraft velocity vector |
| $\mathbf{x}$ | [km] | Spacecraft position vector |
| $\alpha$ | [-] | Percentage to compute departure time |
| $\beta$ | [-] | Percentage to compute DSM |
| $\delta_{\Delta V_0}$ | [rad] | In-plane angle of vector $\Delta V_0$ |
| $\boldsymbol{\Delta P}$ | [kg m/s] | Linear momentum variation |
| $\Delta V$ | [km/s] | Velocity variation of a space manoeuvre |
| $\mu_E$ | [km$^3$/s$^2$] | Earth gravitation constant |
| $\mu_{Sun}$ | [km$^3$/s$^2$] | Sun gravitation constant |
| $\rho_{NEO}$ | [kg/m$^3$] | NEO density |
| $\boldsymbol{\rho}$ | [km] | Relative distance between spacecraft and NEO |
| $\psi_{\Delta V_0}$ | [rad] | Out-of-plane angle of vector $\Delta V_0$ |
| $\Omega$ | [rad] or [deg] | Right ascension of the ascending node |
| $\omega$ | [rad] or [deg] | Argument of perigee |

# 1 Introduction

Asteroids are remnants of the formation of our solar system. They can be distinguished from the composition, the dimension and the type of orbit they follow around the Sun. The comets and in particular the asteroids with a perihelion less than 1.3 astronomic units are the so-called Near-Earth Objects [15].

Probably the most famous one is the Chicxulub asteroid that is thought to have been the cause one of the largest mass extinctions, the extinction of the dinosaurs. But other examples and most recent ones are the Tunguska asteroid (1908) that flattened 2,000 $km^2$ of forest and the one in Chelyabinsk (2013) that shattered glasses and damaged buildings causing thousands of injured. In the the Tunguskal and Chelyabinsk event, the asteroid did not even reach the ground; only the air-burst, due to the explosion in the atmosphere, was enough to produce the described effects [12].

Nowadays, about 800,000 asteroids are known in the solar system and 22,000 of them are registered as NEOs. Figure 1.1 from [12], shows the frequency of impact, the energy and the number of NEOs with varying dimensions. The ones with a diameter larger than 1 kilometer can be surveyed; they are less than 1,000 and none of them is currently a threat for the Earth. The population of the asteroids grows as their size decreases and they become more difficult to be spotted. It is estimated that the percentage of the discovered asteroids with diameter between 300 and 1.000 meters, is 77%; this percentage drops down to 16% for asteroids with dimensions 100-300 m. Instead, the ranges between 0-30 and 30-100 m, that count millions of objects, must be analysed and studied more, since less than 1% of the estimated population is catalogued nowadays.

Moreover, the frequency of impact with the Earth goes with the size of the population. The frequency can go from one impact per year for 1 m diameter asteroids to one impact every 10 years for diameter equal to 10 m. It becomes of thousands and millions of years for asteroids with diameter of 100 m and greater than 1 km respectively.

In the study [11], the effects of an impact with the Earth of an asteroid in the range 10-300 m are modeled. A meteor of 30 m can cause damage to buildings with the generated blast overpressure. When the dimension of the asteroid becomes greater than 50 m, the event passes from a "aerial meteor explosion", that is when the meteor explodes at a height above 10 km, to a "surface meteor explosion" like the Tunguska event. Therefore, the most dangerous asteroids are the one in the range 30-100 meter size, because they are not covered by surveys and their frequency of hitting Earth is very high compared to the kilometer size asteroids.

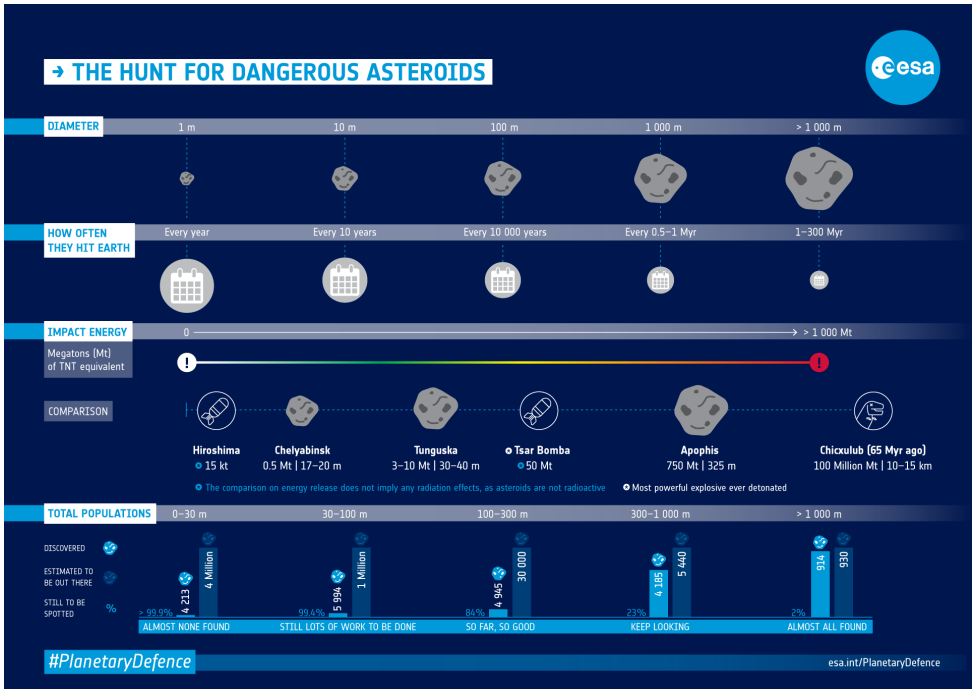


**Figure 1.1:** Asteroids population dimension, frequency of impact, energy of impact and percentage discovered from *Asteroid danger explained*[1].

## 1.1 INTERNATIONAL CO-OPERATION

Several agencies are now involved in observation campaigns to survey unknown near-Earth objects. In particular, the European Space Agency (ESA) established the NEO Coordination Centre (NEOCC) [13]; it has base in Frascati, Italy, and its aim is to coordinate and contribute to the discovery of new objects and to assess their threat. This is done by propagating their orbit and estimating their mass and dimension starting from the observed absolute magnitude. Also, NASA has the NEO observation program that counts several observatories and the CNEOS (Center for Near-Earth Object studies) [14].

In 2013, two organisations were established by the United Nations Committee on the Peaceful Uses of Outer Space: the International Asteroid Warning Network (IAWN) and the Space Mission Planning Advisory Group (SMPAG) [10]. ESA is part of this group together with the space agencies of the major countries like NASA, ASI, CNES, DLR, JAXA. IAWN is a network that links all the institutions responsible of discovering and monitoring the NEO and their potential threats. The main purpose of SMPAG is to exchange information between the partners and develop researches and missions to mitigate threat scenarios.

## 1.2 STATE OF THE ART

Here, a review of the literature concerning past works on the deflection of asteroids is performed. Starting from the available technologies to redirect a NEO, then moving to the main missions that were design for this purpose.

[1]Asteroid danger explained - ESA - `https://www.esa.int/ESA_Multimedia/Images/2018/06/Asteroid_danger_explained`, retrieved on 1/05/2020.

### 1.2.1 How to redirect an asteroid

Following a study of the NASA [26], the possible techniques to redirect an asteroid can be divided in two categories: impulsive techniques and slow push techniques. The first category includes: conventional explosives, nuclear explosives and kinetic impactors. The explosives can be divided in four types:

- "standoff detonation" when the bomb explodes in proximity of the asteroid; it is the less efficient among the four types but it requires only information about the orbit and mass of the target;
- "surface detonation" when the charge explodes on contact with the surface of the target; it is the most efficient together with the next two options, but requires additional information on the physical properties of the asteroid;
- "delayed detonation" consists in landing on the surface of the asteroid and waiting the optimal deflection time;
- "subsurface detonation" when the charge penetrates the target before the explosion.

The charge can be a conventional explosive or a nuclear device; the conventional explosives exhibit the worst efficiency in deviating a NEO. Instead, nuclear devices can be the first choice in terms of energy delivered per unit mass. On the other hand, the use of nuclear charges it is subjected to restrictions and requires international cooperation. Lastly, the kinetic impactors are between the conventional explosives and nuclear devices in terms of efficiency and they especially suffer from the porosity, elasticity and composition of the asteroid. However, they are the safest and highest technology Readiness Level (TRL) options humankind has to redirect an asteroid.

Moving to the "slow push" technique, the alternatives are:

- "Focused solar": it uses a large mirror to focus solar radiation on a precise spot on the surface of the asteroid causing the evaporation of the material and therefore a net thrust;
- "Pulsed laser": same approach as the focused solar technique but the radiation is generated on-board the spacecraft;
- "Mass driver": the spacecraft lands on the asteroid, mines the surface and ejects the extracted material at high velocity generating a momentum transfer [6];
- "Gravity tractor": a big spacecraft flies near the asteroid and exploit the mutual attraction with the asteroid to deviate its trajectory;
- "Asteroid tug": the spacecraft attaches to the target and pushes it with the propulsion system. It is the one with highest performance but requires detailed characterisation of the asteroid;
- "Enhanced Yarkovsky effect": the spacecraft changes the albedo of a rotating asteroid and the radiation coming out the heated material generates a net force.
- Electric sail: metallic conducting tethers are placed on the equator of the NEO; using an electron gun an electric potential is generated between the tethers. This electric field interacts with the solar wind protons generating a thrust [27].

All the slow push techniques could be suitable in the cases when the necessary change in velocity is small and can be applied over several years or even decades and when the asteroid is less than 200 meters in diameter.

### 1.2.2 Past and future missions

The main missions to NEO are now presented; some of them have already terminated, others are still in orbit around the asteroid at the time this thesis is written, others are planned for near future. However, till now, no missions have ever tried to impact with a Near Earth Object.

#### 1.2.2.1 OSIRIS-Rex

The first mission analysed is OSIRIS-Rex developed by NASA [23]. The acronym stands for Origins, Spectral Interpretation, Resource Identification, Security - Regolith Explorer. The spacecraft was launched on September 8, 2016 toward the asteroid Bennu. The mission objectives were:

- Return to Earth and analyse samples from the asteroid;
- Provide direct observation of Bennu;
- Map its composition;
- Measure the effect of sunlight on the orbit (Yarkovsky effect);
- Study the layer of regolith at the sampling site.

In December 2018 the spacecraft arrived to asteroid Bennu and started gathering the science. The study of the asteroid will last until March 2021 when the departure window for Earth will open. In September 2023 a capsule containing the samples will enter Earth's atmosphere.

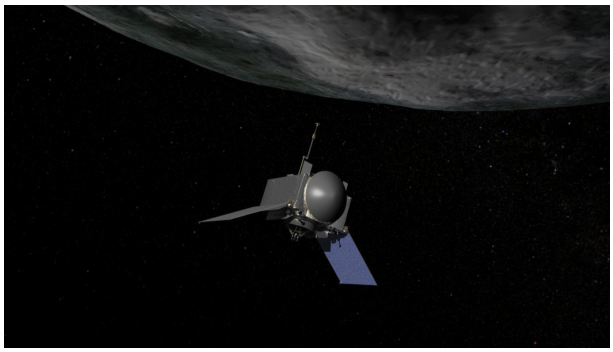

**Figure 1.2:** Artist concept of OSIRIS-REx at BENNU from *OSIRIS-REx images*[2].

#### 1.2.2.2 Hayabusa and Hayabusa 2

Hayabusa was developed by JAXA [22]. It was launched on May 9, 2003 toward the asteroid Itokawa reached in 2005. There the spacecraft studied Itokawa's surface and collected samples. After less than two years it left the asteroid and on June 13, 2010 ended the mission dropping its capsule in Earth's atmosphere.

Hayabusa 2 is the son of Hayabusa and was launched in 2014 toward the asteroid Ryugu [21]. It arrived at the asteroid in 2018 and started to gather the science. This time an impact with a copper projectile was also performed, in order to create a crater on the surface of the asteroid where the spacecraft dived to collect sub-surface samples. This mission will provide more information about the internal structure of the asteroids. It is expected to return to Earth in late 2020.

[2]OSIRIS-REx images - NASA, Karl Hille -`https://www.nasa.gov/image-feature/osiris-rex-at-bennu`, retrieved on 1/05/2020.

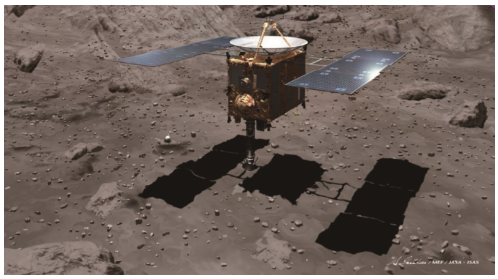

**Figure 1.3:** Illustration of Hayabusa at Itokawa from *Asteroid Explorer "HAYABUSA" Ion Engine Anomaly*[3].

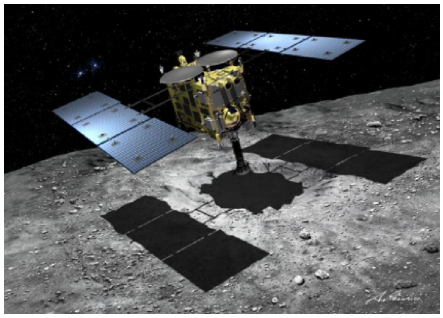

**Figure 1.4:** Illustration by Akihiro Ikeshita of Hayabusa 2 at Ryugu from [21].

#### 1.2.2.3 Don Quijote

It was a European plan to prove the capability of deflecting an asteroid and measure the momentum transfer and the consequent variation in orbital parameters [19]. The main design consisted of the impactor called Hidalgo and the orbiter, Sancho, that had the task of studying the asteroid and collect the data of the impact. This mission was substituted by the AIDA mission born from the collaboration between ESA and NASA.

#### 1.2.2.4 AIDA

The Asteroid Impact and Deflection Assessment mission is a cooperation between NASA and ESA. It will be the first mission to demonstrate the capability of mitigating asteroid impact hazard using a kinetic impactor [20].

The mission, represented in figure 1.5, is divided in two phases. The first mission is the Double Asteroid Redirection Test (DART): it is composed by the kinetic impactor that will be launched in 2021 and will hit the moon of the asteroid Didymos in 2022. It is selected to hit the secondary body of this binary system, because it is easy to measure the variation of orbit period around the primary body also from Earth observatories.

The second part is the Hera mission: it will reach Didymos few years after the impact and determine the momentum transfer to Didymoon. Moreover, it will collect also data that will be critical to estimate the beta parameter, that is the ratio of momentum transferred over the incident momentum.

## 1.3 PAST WORKS ON THREATENING ASTEROIDS MITIGATION

The study and observation of the overwhelming number of NEOs in our solar system, has pushed the research in the last 20 years, to design methods to deviate possible hazardous asteroids, in particular strategies based on kinetic impactors.

This thesis starts from the work of Vasile and Colombo [8], where the optimal trajectories to hit different asteroids and predict the optimal direction of the momentum transfer to the NEO to obtain the maximum deviation are computed. Another work by Sanchez and Colombo [7], generated a random sample of possible NEOs to study the influence of the target's orbit on the deviation achievable.The advantage of the analysis in these works is that to study the performance of the kinetic impactor

[3]Asteroid Explorer "HAYABUSA" Ion Engine Anomaly - JAXA - `http://www.isas.jaxa.jp/e/topics/2009/1109.shtml`, retrieved on 1/05/2020.

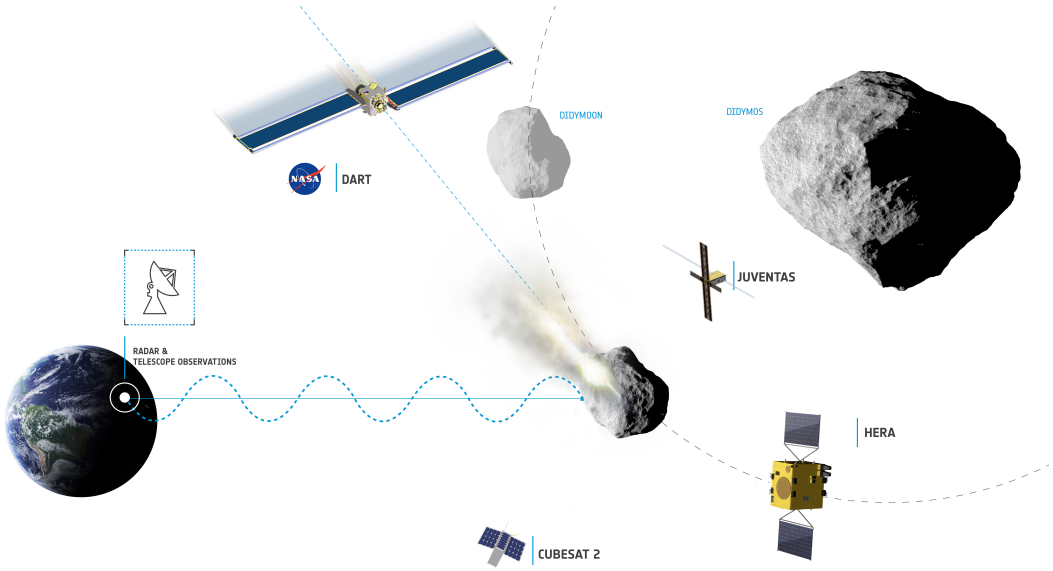


**Figure 1.5:** Illustration of the AIDA mission from *Asteroid Impact & Deflection Assessment (AIDA) collaboration*[4].

strategy from a general view point, so that their results can be applied to specific cases.

On the other hand, the article by Colombo et al. [5], presents a detailed design of a possible kinetic impactor mission and the optimisation of the trajectory on two potential threat asteroids; one of them is also the target of this thesis. In this way, the results obtained in this thesis can be supported and compared with the results of [5].

Other studies taken into account, are the thesis of Petit [3] and Bolsi [2]; the first one focused on deviating the asteroid such that it avoids the close-encounter with the Earth but also minimises the risk of a resonant return on the Earth path. The second work instead, found the optimal impact strategy when the spacecraft performs fly-by of the Earth, Venus or Mars.

The final work considered is the thesis of Giovanni Purpura [1], in which he developed a control strategy based on the image processing of the NEO and tested it with a real-time simulation of the last 2000 seconds before the impact with the asteroid.

The limit of the cited works is that none of them took into account if the spacecraft is capable of hitting the asteroid, in fact all of them supposed a perfect impact with the target. From this consideration and from the model designed in the thesis of Purpura [1] and here adapted, this thesis aims at including in the optimisation process also a simulation in real time of the approaching phase of the spacecraft towards the target.

## 1.4 PURPOSE OF THIS WORK

The purpose of this work is to create a tool that from the orbit and dimension of a NEO and the characteristics of a designed spacecraft, it is capable of optimising the trajectory of the impactor. The

[4]Asteroid Impact & Deflection Assessment (AIDA) collaboration - Esa, Science Office - `https://www.esa.int/ESA_Multimedia/Images/2019/01/Asteroid_Impact_Deflection_Assessment_AIDA_collaboration#.XrOP_9zhCxd.link`, retrieved on 1/05/2020.

novelty is that the real-time simulation of the approaching phase to the asteroid is embedded in the optimisation process. The result will be a trajectory with a probability of impacting the target and an efficiency of the impact itself. Eventually, it could become a tool to evaluate different guidance and control algorithms and whether a kinetic impactor strategy is the best choice to deviate a particular threatening asteroid. All of this is done, taking as reference case a well known and already studied NEO.

## 1.5 WORK OUTLINE

First of all, in chapter 2 the physical properties of the asteroid and its model are presented; then, the impactor is presented with the description of its trajectory and the guidance and control it performs. Moving to chapter 3, how the impact with the asteroid is modeled and the computation of the efficiency are explained. There is also a presentation of the method to propagate the asteroid orbit after the impact. In chapter 4, a brief analysis of the behaviour of the control algorithm is conducted when the dimension of the asteroid changes and when different cameras are installed on the spacecraft.
In chapter 5, the different types of trajectory tested, the optimisation processes and the results obtained are described. Finally, in chapter 6, a recap of the main results is given together with some suggestions for future work.

# 2 Mission analysis and Guidance Control

In this chapter, firstly are described the asteroids characteristics and model; then is the turn of the spacecraft main parameters. Finally, the mission is analysed in its different parts and is presented a description of the guidance and control algorithm mounted on the spacecraft.

## 2.1 Asteroid's physical properties

Asteroids vary a lot in composition, surface properties, shape and dimension. In this section, the assumptions made and the properties assigned to the asteroid are reported .

Let's start from the mean density. In [18], the values of density for different classes of asteroids are presented. In particular, the standard NEA density is given. It has been obtained from a weighted mean of the population of asteroids and their absolute magnitude; very few asteroids have this specific value, however, it is the value that can better represent all types at the same time. Therefore, the mean density is $\rho_{_{NEO}} = 2600\ \mathrm{kg/m^3}$.
In the same way, a standard albedo ($Alb_{NEO}$) equal to 0.154 is obtained.

Passing to the shape of the asteroid, it is hard to define a general geometry representative of the entire population, because asteroids can have very particular and weird shapes. To have a simple and manageable geometry an ellipsoidal shape is selected. It is defined by three diameters A, B, C that are the three principal axes of the ellipsoid. Equation 2.1 describes an ellipsoid in a 3D reference frame centered in its origin and aligned with its principal axes.

$$\frac{x^2}{a^2} + \frac{y^2}{b^2} + \frac{z^2}{c^2} = 1 \tag{2.1}$$

where a, b and c are the semi-major and semi-minor axes (half of the diameters A, B, C). The volume of this geometry is:

$$V_{NEO} = \frac{4}{3}\pi abc = \frac{\pi}{6}ABC \tag{2.2}$$

From the volume of the ellipsoid and the mean density it is possible to obtain the mass of the NEO:

$$m_{NEO} = \rho_{NEO} V_{NEO} \tag{2.3}$$

## 2.2 Three dimensional model

A detailed 3D model of asteroid 2010RF12 is not available because it is a faint object. Therefore, the 3D model of asteroid 101955 Bennu, shown in Figure 2.1 and available on the NASA 3D resources site [16], is used.

This model is reconstructed from the radar observations of this object that has almost a spherical shape with mean diameter equal to 550 m; it is provided in the format .STL and it is visualised with the software Blender®. It is a free software to model and rendering 3D shapes; it is used to generate a realistic image of the NEO providing the position of the light source, that in this thesis is represented the Sun, and setting the position of the spacecraft on which the camera is mounted.

Moreover, this software has a scale option that can be used to stretch or shrink the 3D model of the asteroid along the three axes x, y, z. In this way, it is possible to generate an asteroid with a general ellipsoidal shape knowing the ratio between its principal axes and Bennu's ones. The minimum scale factor obtainable for this model is equal to 0.01; such a value will generate an object with mean diameter equal to 5.5 m that is enough for the purpose of this thesis.

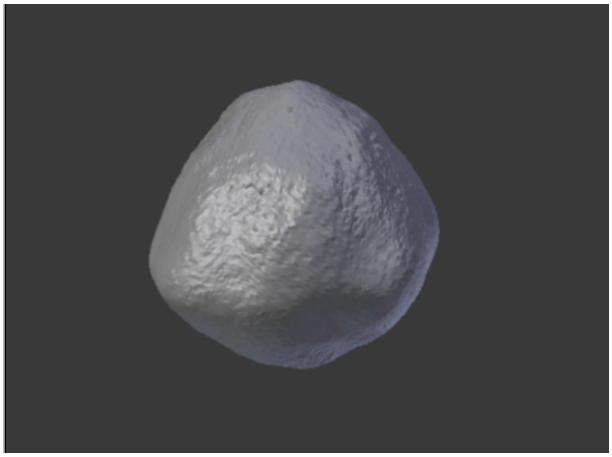

**Figure 2.1:** 3D model of Bennu from [16].

## 2.3 TARGET SELECTION

For this thesis, an asteroid must be selected as a test case. NEAs orbit can vary a lot from one asteroid to another, hence any choice could be not very representative of the entire population. However, without loss of generality, the asteroid 2010 RF12 is selected for two main reasons: firstly, it has one of the highest probabilities of hitting the Earth, so it is a realistic case study. From NEODyS-2 risk pages [17], it has 6.57% probability of impact on 5 September 2095 and could generate an energy in the order of ten kilotons, like the Hiroshima bomb. Secondly, other works studied this case and can be compared with the results obtained in this thesis [5].

2010RF12 is a small asteroid with a diameter between 4 and 12 meters. Before 2095, this asteroid will undergo several close encounters with Earth that will change slightly its orbital parameters. The NEODyS-2 site provides the current orbital parameters. However, this work uses the parameters from [5] that takes into account the close encounters in 2059 and 2084 and they are reported in Table 2.1.

In Figure 2.2, the orbit of the NEO with its main characteristics is represented. The orbit of the NEO can be characterised by the Minimum Orbital Intersection Distance (MOID), that is the minimum separation between the asteroid's orbit and the Earth's orbit. The MOID is computed through a numerical minimisation that uses as decision variables the mean anomaly of the NEO and of the Earth. The user provides the initial guess values of the decision variables; then, at each step, the algorithm selects two new values for the mean anomalies and, from the other Keplerian parameters, it computes

| | Value | Units |
|---|---|---|
| a | 1.057 | AU |
| e | 0.187 | - |
| i | 0.91 | deg |
| Ω | 162.8 | deg |
| $\omega$ | 267.1 | deg |

**Table 2.1:** 2010RF12 Keplerian parameters in 2095 from [17].

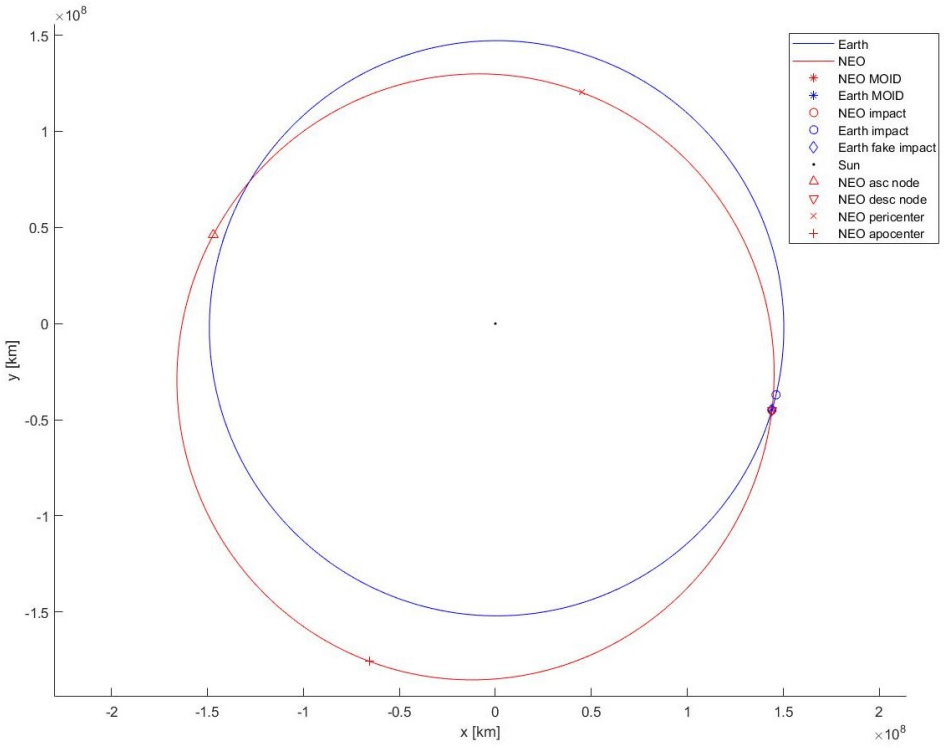


**Figure 2.2:** 2010RF12 and the Earth's orbit.

the correspondent two positions on the orbit of the NEO ($\mathbf{X_{NEO}}$) and of the Earth ($\mathbf{X_{Earth}}$) expressed in heliocentric reference frame. Then, the algorithm computes the fitness function $J$, that is the distance between these two points, with Eq. 2.4.

$$J = ||\mathbf{X_{NEO}} - \mathbf{X_{Earth}}|| \tag{2.4}$$

The value of the fitness function converges to the MOID and the correspondent mean anomaly of NEO and Earth are retrieved. This procedure is repeated four times with different and well separated initial guesses in order to guarantee that the algorithm has converged to the global minimum.

Once the mean anomaly of the MOID is obtained, it is possible to reconstruct the time at which the NEO is at the MOID starting from the possible impact epoch $t_{MOID}$ (2095). However, when the asteroid is at the MOID the Earth is not, but it can be slightly before or after that point. Therefore, to consider the worst possible case, the Earth is placed at the MOID using a synthetic true anomaly.

It is possible to compute the relative velocity between the NEO and the Earth at the MOID ($\mathbf{v}_\infty$) and then the radius of the pericentre of the hyperbolic path that the asteroid follows when passing

near the Earth [5].

$$r_p = \sqrt{\frac{\mu_E^2}{||\mathbf{v}_\infty||^4} + ||\mathbf{b_{NEO}}||^2} \quad - \quad \frac{\mu_E}{||\mathbf{v}_\infty||^2} \tag{2.5}$$

where $\mu_E$ is the Earth's gravitational constant equal to $3.9860 \times 10^5$ km$^3$/s$^2$ and $\mathbf{b_{NEO}}$ is the relative position NEO-Earth transformed in the b-plane reference frame. The b-plane is a local reference system represented in Figure 2.3, where the x axis is aligned with $\mathbf{v}_\infty$, the y axis is obtained from the cross product between Earth's velocity and x axis, and the z axis is obtained from the right hand rule. The axes are computed in Eq. 2.6, where $\mathbf{V_E}$ is the velocity of Earth in the heliocentric reference frame [8].

$$\hat{\mathbf{x}}_\mathbf{b} = \frac{\mathbf{v}_\infty}{||\mathbf{v}_\infty||} \qquad \hat{\mathbf{y}}_\mathbf{b} = \frac{\mathbf{V_E} \times \hat{\mathbf{x}}_\mathbf{b}}{||\mathbf{V_E} \times \hat{\mathbf{x}}_\mathbf{b}||} \qquad \hat{\mathbf{z}}_\mathbf{b} = \hat{\mathbf{y}}_\mathbf{b} \times \hat{\mathbf{x}}_\mathbf{b} \tag{2.6}$$

Eq. 2.7 represents the transformation from Cartesian reference frame to b-plane; the subscripts $car$ and $b-plane$ mean that the position vector $\mathbf{X}$ is expressed respectively in Cartesian reference frame and b-plane frame.

$$\mathbf{X_{b-plane}} = \begin{bmatrix} \hat{\mathbf{x}}_\mathbf{b} & \hat{\mathbf{y}}_\mathbf{b} & \hat{\mathbf{z}}_\mathbf{b} \end{bmatrix} \mathbf{X_{Car}} \tag{2.7}$$

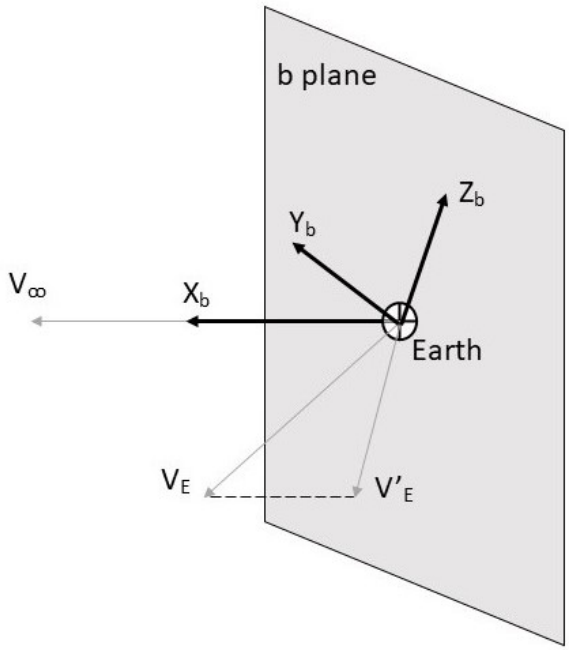


**Figure 2.3:** Representation of the b-plane from [8].

## 2.4 KINETIC IMPACTOR MISSION

In this section, the main parameters that define the spacecraft and the mission are described. Then, the trajectory the spacecraft follows will be analysed. It is divided in two phases: the coast phase that begins from the departure from Earth and terminates when the asteroid becomes visible in the camera of the spacecraft. The second part is the navigation phase, where the trajectory of the spacecraft is the result of a real-time simulation in which the control algorithm guides the spacecraft until the impact with the asteroid.

### 2.4.1 Mission design parameters

The main fixed parameters describing the spacecraft and the whole mission are:

- The total mass of the spacecraft;
- the structure and propellant mass fraction;
- the specific impulse of the propulsion system (Isp);
- the maximum excess velocity provided by the launcher;
- the maximum thrust of the control thrusters mounted on the spacecraft.

The total mass of the spacecraft is directly proportional to the momentum transfer to the asteroid and therefore, to the deviation achievable as shown by [2] and [5]. Hence, the higher the mass the better the results. Studies were made, like [2] and [5], where the mass of the spacecraft varies between 100 kg and up to 8 tons. Therefore, for this thesis a mass for the spacecraft equal to 500 kg is selected. In addition, this value is comparable with the mass of the spacecraft used in the Simulink® model developed in [1], so that the control capability of the thrusters selected in the model is not compromised.

Regarding the structure mass fraction, like in [8], it is assumed to be 20% of the total mass. Another 10% of the total mass is addressed to the tank and propulsion system. The rest of the mass is considered to be propellant, obtaining a propellant mass fraction of 0.7.

Considering the Isp of the spacecraft, the value of 300 s is selected, that is a typical value for a bi-propellant propulsion system. From the Tsiolkovsky equation and the propellant mass fraction, it is possible to obtain the maximum available $\Delta V$ for the spacecraft :

$$\Delta V_{max} = -Isp\ g_0\ \ln\left(\frac{(1-0.7)m_{sc_0}}{m_{sc_0}}\right) \simeq 3.5\ \frac{km}{s} \tag{2.8}$$

Regarding the launch, the maximum escape velocity provided by the launcher is $\Delta V_{launch} = 3$ km/s. This value is typical for interplanetary missions and depends on the performance of the launcher and the total mass of the spacecraft. Therefore, if in future works it will be necessary to increase the mass of the spacecraft, it is important to take into account the reduction in total excess velocity.

Finally, for the thrusters the maximum output is set to 5 N, because in [1] it was demonstrated that this value is enough to control a spacecraft of half a ton.

### 2.4.2 Impactor's trajectory

In this section the trajectory that the spacecraft follows till the encounter with the asteroid will be analysed. The trajectory of the spacecraft can be divided in two phases: the coast phase and the navigation phase. For the coast phase this thesis follows the work in [2]; while for the navigation phase the work in [1] is taken as reference.

#### 2.4.2.1 Coast phase

The coast phase starts with the departure from Earth's orbit. It is assumed that, at departure time $t_0$, the spacecraft position coincides with Earth's one and its velocity is the velocity of the Earth plus the excess velocity provided by the launcher. This velocity can be computed in two ways: it can be the result of a Lambert problem between the initial position and the position of impact with the asteroid when a

certain time of flight is defined; or it can be defined as a vector in the heliocentric frame. Knowing these initial conditions, it is possible, through the Keplerian equations, to propagate in time position and velocity of the spacecraft. Similarly, are propagated in time position and velocity of the asteroid knowing its Keplerian parameters at time t0 from the ephemerides of the object.

During the coast phase, the spacecraft can perform pre-determined Deep Space Manoeuvres (DSM) to correct the orbit [2]. The coast phase terminates when the camera of the spacecraft spots for the first time the asteroid.

#### 2.4.2.1.1 Spot time

The spot time is when the light coming from the asteroid is enough that the pixel in the camera is illuminated and the signal is well identifiable with respect to the background noise. This condition depends on the geometry of the problem, as arrangement Sun-asteroid-spacecraft and the percentage of asteroid illuminated; moreover, it also depends on the aperture of the camera, its exposure time, the sensibility and noise of the detector.

It is assumed that, in order to distinguish a signal from the noise, it is required a Signal-to-Noise Ratio (SNR) of at least 5. The SNR is modelled with equation 2.9 [42].

$$\begin{gathered} SNR = \frac{G\, s_{NEO}}{\sqrt{B}} \\ B = F^2 \cdot G \cdot (s_{NEO} + s_{SL} + s_{DC}) + \sigma_{RON}^2 + \sigma_{OCN}^2 + \sigma_{QN}^2 \end{gathered} \tag{2.9}$$

where G is the detector gain, $s_{NEO}$ is the signal coming from the object onto the pixel and $\sqrt{B}$ is the noise. Taking as reference the datasheet of the CCD S12101 produced by Hamatstu® [43], the noise is composed by:

- noise factor of the detector $F = \sqrt{2}$.
- gain of the detector $G = 1$.
- readout noise $\sigma_{RON} = 1e^-$, that is caused by the conversion of the electrons collected on the pixel into a analog voltage.
- quantisation noise $\sigma_{QN} = \frac{0.7cap}{2^N\sqrt{12}}$, with maximum charge capacity of a pixel $cap$ = 80 ke$^-$, and number of bits $N_{bits} = 12$ that. This noise is due to the discretisation of the analog signal in a digital signal.
- off-circuit noise $\sigma_{OCN} = 8e^-$ caused by the other instrumentation on the spacecraft.
- dark current noise $s_{DC} = k_{DC}T_{exp}$ that depends on the exposure time and it is the consequence of the temperature of the CCD. At an operating temperature between -10 and 0 °C, from Figure 2.4 $k_{DC} = 5e^-/s$.
- straylight noise $s_{SL} = k_{SL}T_{exp}$ is due to light coming to the CCD that does not follow the designed path. It is difficult to estimate, therefore the $k_{SL}$ = 5 e$^-$/s to be comparable with the dark current noise.

Assuming that during the exposure time the spacecraft is not rotating so that the asteroid is always on the same pixel, the signal coming from the asteroid is computed following [41].

$$s_{NEO} = ne^-_{NEO}\sqrt{T_{exp}} \tag{2.10}$$

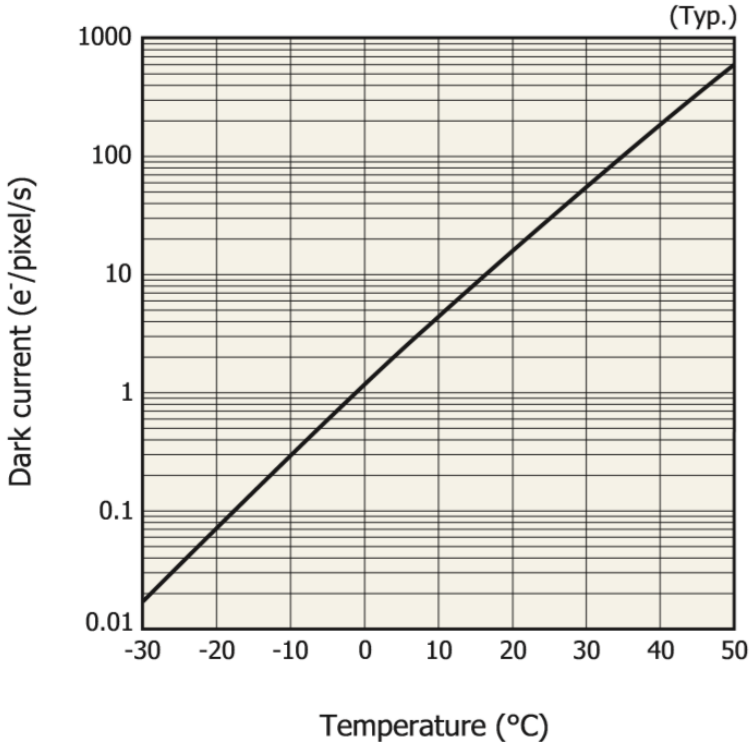


**Figure 2.4:** Dark noise as a funtion of the temperature of the CCD S12101 from [43].

where $ne^-_{NEO}$ is the number of electrons generated per unit second. It is obtained multiplying the quantum efficiency of the detector times the number of photons coming from the NEO that is:

$$np_{NEO} = \frac{\xi \, D_{ap}^2 \, F_{NEO}}{16 \, L^2} \tag{2.11}$$

where:

- $\xi$ is the collection efficiency of the telescope, assumed = 0.1 [41].
- $D_{ap}$ is the aperture of the telescope.
- $L$ is the distance between spacecraft and NEO.

$F_{NEO}$ is the flux of photons arriving from the Sun and reflected by the asteroid [41]:

$$F_{NEO} = A_{NEO} \, Alb_{NEO} \, F_{Sun} \, f_{lit} \tag{2.12}$$

where:

- $A_{NEO}$ is the surface of the asteroid. In the case of an ellipsoidal asteroid it is taken the minimum diameter and the asteroid is treated as a spherical one; in this way the number of photons is underestimated.
- $Alb_{NEO}$ is the reflection coefficient of the asteroid, assumed = 0.154 as in section 2.1.
- $F_{Sun}$ is the photon flux coming from the Sun at 1 AU for the corresponding range of the detector, that is 250-1050 nm.

- $f_{lit}$ is the illuminated fraction of asteroid.

$f_{lit}$ is computed knowing the angle Sun-NEO-spacecraft $\psi$ that is represented in Figure 2.5.

$$f_{lit} = \frac{\pi - \psi}{\pi} \tag{2.13}$$

This fraction is 1 when the spacecraft is between the Sun and the asteroid (the spacecraft has the Sun

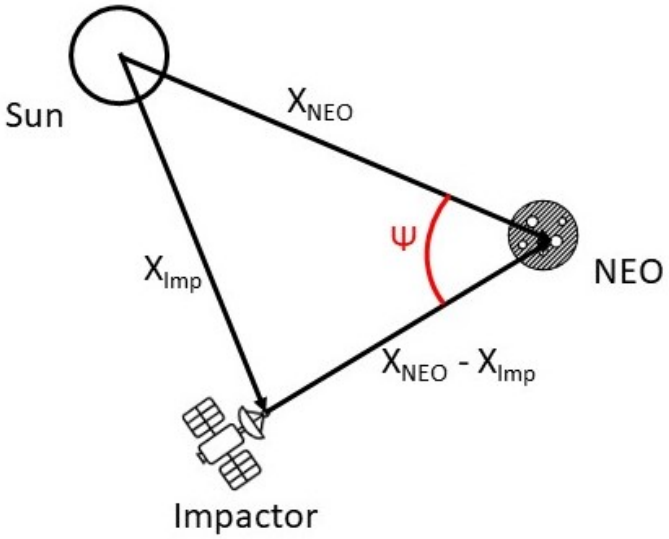


**Figure 2.5:** Representation of the Sun angle $\psi$.

behind), while it is 0 when the asteroid is between Sun and spacecraft (the spacecraft has the Sun ahead).

Knowing the nominal conditions (position and velocity) of spacecraft and NEO at impact, the orbits are integrated back in time until the value of SNR passes from a value higher than 5 to a value lower than 5, that is the selected threshold to distinguish a signal from the noise. When this condition is met, the navigation phase starts.

#### 2.4.2.2 Navigation phase

The navigation phase is different from the coast phase because this part is simulated via a real time model using Simulink®. The model used is the one provided by the thesis of Purpura [1]. Inside this model can be distinguished 4 parts: the dynamics of the spacecraft and asteroid, the sensors part, the filter and the controller. The model is adapted for the purpose of this thesis. In particular, the possibility to change the dimension of the asteroid and the initial conditions of spacecraft and asteroid is added. On the other hand, the part that describes the rotational dynamics of asteroid and spacecraft is discarded in order to have a faster simulation time, useful for the optimisation process.

##### 2.4.2.2.1 Asteroid and spacecraft translational dynamics

Therefore, this model contains only the translational dynamics of impactor and NEO. In order to express the dynamics, it is necessary to introduce three different reference frames. The first is the

heliocentric ecliptic frame represented in Figure 2.6; it is a inertial frame that has origin in the Sun and the x axis points towards the vernal equinox, the z axis is perpendicular to Earth's ecliptic plane and the y axis is obtained with the right-hand rule.

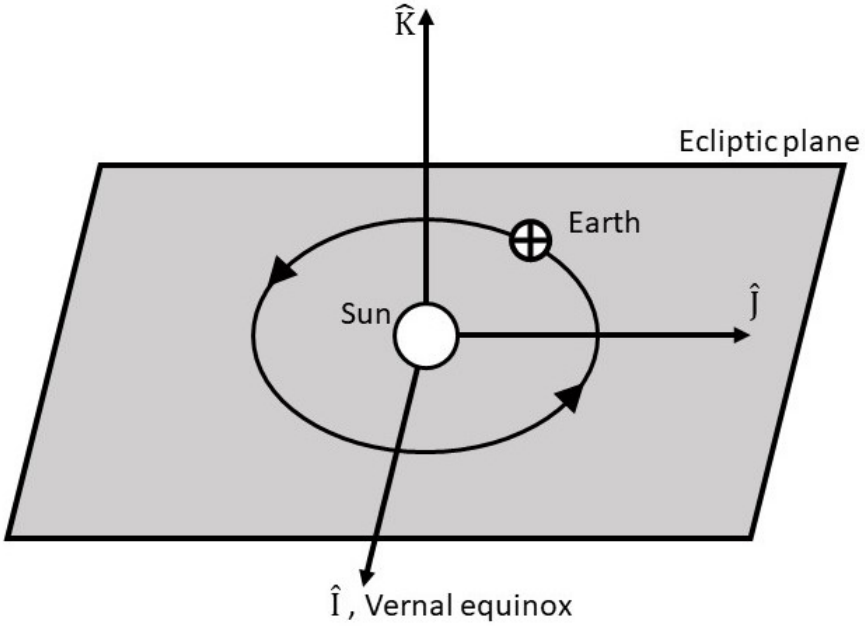


**Figure 2.6:** Heliocentric reference frame.

The second reference system is the Hill's rotating frame. This frame is centred in the asteroid with the $\hat{\mathbf{r}}$ axis aligned with the NEO's position vector with respect to the Sun ($\mathbf{r_a}$), the $\hat{\mathbf{h}}$ axis perpendicular to the orbital plane of the asteroid and $\hat{\boldsymbol{\theta}}$ axis obtained again with the right-hand rule like it is shown in Figure 2.7. The dynamics of the spacecraft is expressed in this frame.
From position of the NEO with respect to the Sun $\mathbf{r_a}$ and its orbital velocity $\dot{\mathbf{r}}_\mathbf{a}$ the axis of the Hill reference frame are obtained with the equations 2.14.

$$\hat{\mathbf{r}} = \frac{\mathbf{r_a}}{||\mathbf{r_a}||}, \qquad \hat{\boldsymbol{\theta}} = \hat{\mathbf{h}} \times \hat{\mathbf{r}}, \qquad \hat{\mathbf{h}} = \frac{\mathbf{r_a} \times \dot{\mathbf{r}}_\mathbf{a}}{||\mathbf{r_a} \times \dot{\mathbf{r}}_\mathbf{a}||} \tag{2.14}$$

Since this frame in non-inertial, because it rotates together with the asteroid around the Sun with an angular velocity $\mathbf{w} = \dot{\theta}\,\hat{\mathbf{h}}$ with $\theta$ being the true anomaly, the versors $\hat{\mathbf{r}}$ and $\hat{\boldsymbol{\theta}}$ are time dependent and governed by the ordinary differential equations (ODE) expressed in the system 2.15 [1].

$$\begin{cases} \dot{\hat{\mathbf{r}}} = \mathbf{w} \times \hat{\mathbf{r}} = \dot{\theta}\,\hat{\boldsymbol{\theta}} \\ \dot{\hat{\boldsymbol{\theta}}} = \mathbf{w} \times \hat{\boldsymbol{\theta}} = -\dot{\theta}\,\hat{\mathbf{r}} \end{cases}$$

$$\begin{cases} \ddot{\hat{\mathbf{r}}} = \ddot{\theta}\,\hat{\boldsymbol{\theta}} + \mathbf{w} \times \dot{\theta}\,\hat{\boldsymbol{\theta}} = \ddot{\theta}\,\hat{\boldsymbol{\theta}} - \dot{\theta}^2\,\hat{\mathbf{r}} \\ \ddot{\hat{\boldsymbol{\theta}}} = -\ddot{\theta}\,\hat{\mathbf{r}} + \mathbf{w} \times (-\dot{\theta}\,\hat{\mathbf{r}}) = -\ddot{\theta}\,\hat{\mathbf{r}} - \dot{\theta}^2\,\hat{\boldsymbol{\theta}} \end{cases} \tag{2.15}$$

Given the three versors expressed in the heliocentric frame $\hat{\mathbf{r}}$, $\hat{\boldsymbol{\theta}}$, $\hat{\mathbf{h}}$, the rotation matrix from heliocentric frame to Hill frame is:

$$\mathbf{A_{E/H}} = [\hat{\mathbf{r}} \quad \hat{\boldsymbol{\theta}} \quad \hat{\mathbf{h}}] \tag{2.16}$$

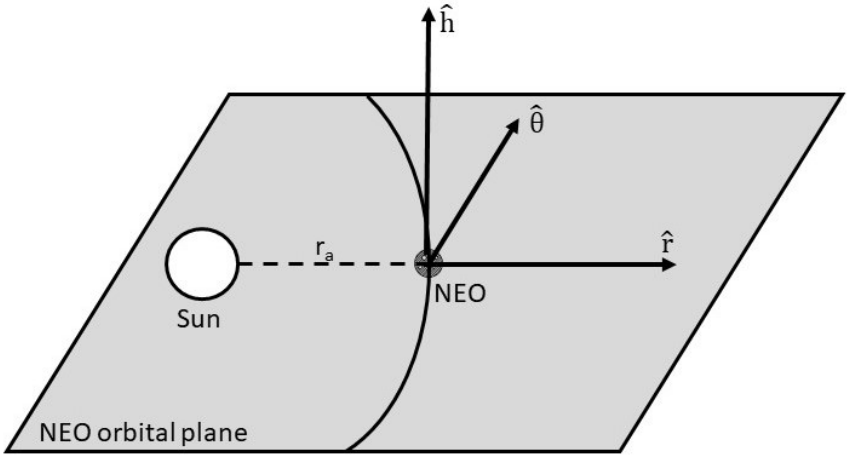


**Figure 2.7:** Hill's reference frame.

The last frame is the body-fixed frame attached to the spacecraft and coincident with its principal moments of inertia. Even if the rotational dynamic of the spacecraft is not described in this simplified model, the information on the orientation of the spacecraft is maintained so that the camera of the spacecraft is always pointed towards the asteroid. The camera is mounted in the opposite direction of the body frame z axis and from the quaternion expressing the orientation of the spacecraft, $\mathbf{q} = [q_w \; q_x \; q_y \; q_z]$, it is possible to recover the rotation matrix from heliocentric frame to the body frame:

$$\mathbf{A_{B/E}} = \begin{bmatrix} q_w^2 + q_x^2 - q_y^2 - q_z^2 & 2(q_x q_y + q_w q_z) & 2(q_x q_z - q_w q_y) \\ 2(q_x q_y - q_w q_z) & q_w^2 - q_x^2 + q_y^2 - q_z^2 & 2(q_y q_z + q_w q_x) \\ 2(q_x q_z + q_w q_y) & 2(q_y q_z - q_w q_x) & q_w^2 - q_x^2 - q_y^2 + q_z^2 \end{bmatrix} \tag{2.17}$$

Now that all the reference frames are introduced, it is possible to write the equations of motion of both NEO and impactor. Assuming that no forces apart the Sun attraction act on the asteroid, the dynamic equations that describe the revolution of the NEO around the Sun are derived from the Newton's gravitation law written in Eq. 2.18.

$$\ddot{\mathbf{r}}_\mathbf{a} = -\frac{\mu}{r_a^2}\hat{\mathbf{r}} \tag{2.18}$$

Where $\mu$ is the Sun gravitational constant equal to $1.32712440018 \times 10^{20}$ m$^3$/s$^2$. Using Eq. 2.15, $\mathbf{r_a}$ is derived two times in order to obtain an expression of $\ddot{\mathbf{r}}_\mathbf{a}$ in Hill's frame as in Eq. 2.19.

$$\begin{cases} \mathbf{r_a} = r_a \, \hat{\mathbf{r}} \\ \dot{\mathbf{r}}_\mathbf{a} = \dot{r}_a \;\; \hat{\mathbf{r}} + r_a \, \dot{\theta} \, \hat{\boldsymbol{\theta}} \\ \ddot{\mathbf{r}}_\mathbf{a} = \left(\ddot{r}_a - r_a \, \dot{\theta}^2\right)\hat{\mathbf{r}} + \left(r_a \, \ddot{\theta} + 2\dot{r}_a \, \dot{\theta}\right)\hat{\boldsymbol{\theta}} \end{cases} \tag{2.19}$$

Substituting this expression of $\ddot{\mathbf{r}}_\mathbf{a}$ in Eq. 2.18 results in:

$$\left(\ddot{r}_a - r_a \, \dot{\theta}^2\right)\hat{\mathbf{r}} + \left(r_a \, \ddot{\theta} + 2\dot{r}_a \, \dot{\theta}\right)\hat{\boldsymbol{\theta}} = -\frac{\mu}{r_a^2}\hat{\mathbf{r}}$$

Since $\hat{\mathbf{r}}$ and $\hat{\boldsymbol{\theta}}$ are orthogonal, this expression can be split in two decoupled non-linear ordinary differential equation of the second order that describe the motion of the NEO around the Sun.

$$\begin{cases} \ddot{r}_a = r_a \, \dot{\theta}^2 - \frac{\mu}{r_a^2} \\ \ddot{\theta} = -2\frac{\dot{r}_a \, \dot{\theta}}{r_a} \end{cases} \tag{2.20}$$

Like for the asteroid, also the dynamics of the spacecraft is determined by the Newton's gravitational law; but this time, in addition to the gravitational force of the Sun, the thrust provided by the spacecraft actuator, represented by the term $\mathbf{T_s}$, is added in Eq 2.21 [1].

$$\ddot{\mathbf{r}}_\mathbf{s} = -\frac{\mu}{r_s^3}\mathbf{r_s} + \frac{\mathbf{T_s}}{m_s} \tag{2.21}$$

$\mathbf{T_s}$ is the control force expressed in the Hill's frame; however the thrust is aligned with and is computed in the body frame. Therefore, the obtained thrust must be transformed from body frame in Hill's frame with Eq. 2.22.

$$\mathbf{T_s}^H = \mathbf{A_{H/E}}\,\mathbf{A_{B/E}}^T\,\mathbf{T_s}^B \tag{2.22}$$

Since the NEO is the target, in Eq. 2.23 the dynamics of the relative position between NEO and impactor expressed in Hill's frame is derived [1].

$$\begin{cases} \boldsymbol{\rho} = \mathbf{r_s} - \mathbf{r_a} = x\,\hat{\mathbf{r}} + y\,\hat{\boldsymbol{\theta}} + z\,\hat{\mathbf{h}} \\ \dot{\boldsymbol{\rho}} = (\dot{x} - \dot{\theta}\,y)\,\hat{\mathbf{r}} + (\dot{y} + \dot{\theta}\,x)\,\hat{\boldsymbol{\theta}} + \dot{z}\,\hat{\mathbf{h}} \\ \ddot{\boldsymbol{\rho}} = (\ddot{x} - 2\dot{\theta}\,\dot{y} - \ddot{\theta}\,y - \dot{\theta}^2\,x)\,\hat{\mathbf{r}} + (\ddot{y} + 2\dot{\theta}\,\dot{x} + \ddot{\theta}\,x - \dot{\theta}^2\,y)\,\hat{\boldsymbol{\theta}} + \ddot{z}\,\hat{\mathbf{h}} \end{cases} \tag{2.23}$$

Using Eqs. 2.23 and 2.18 it is possible to obtain the second derivative of $\mathbf{r_s}$ as follows:

$$\ddot{\mathbf{r}}_\mathbf{s} = \ddot{\boldsymbol{\rho}} + \ddot{\mathbf{r}}_\mathbf{a} = \begin{bmatrix} \ddot{x} - 2\dot{\theta}\,\dot{y} - \ddot{\theta}\,y - \dot{\theta}^2\,x - \frac{\mu}{r_a^2} \\ \ddot{y} + 2\dot{\theta}\,\dot{x} + \ddot{\theta}\,x - \dot{\theta}^2\,y \\ \ddot{z} \end{bmatrix} \tag{2.24}$$

Finally, substituting Eq. 2.24 in Eq. 2.21 the dynamics of the spacecraft relative to the NEO in Hill's frame is:

$$\begin{cases} \ddot{x} = 2\dot{\theta}\,\dot{y} + \ddot{\theta}\,y + \dot{\theta}^2\,x + \frac{\mu}{r_a^2} - \mu\frac{x + r_a}{r_s^3} + \frac{T_{sx}}{m_s} \\ \ddot{y} = -2\dot{\theta}\,\dot{x} - \ddot{\theta}\,x + \dot{\theta}^2\,y - \mu\frac{y}{r_s^3} + \frac{T_{sy}}{m_s} \\ \ddot{z} = -\mu\frac{z}{r_s^3} + \frac{T_{sz}}{m_s} \end{cases} \tag{2.25}$$

The definition of the reference frame is exploited to reconstruct the values of the spacecraft and NEO states at the beginning of the navigation phase. From position $X_{NEO}$, velocity $V_{NEO}$ and true anomaly $\theta_{NEO}$ of the NEO at the spot time, the Hill's reference frame axes $\hat{\mathbf{r}}$, $\hat{\boldsymbol{\theta}}$, $\hat{\mathbf{h}}$ are obtained following Eq. 2.14.

The initial conditions of the ODE for the NEO are summarised in Eq. 2.26. The parameters with the superscript $E$ means that are evaluated in the heliocentric inertial frame.

$$\begin{cases} r_0 &= \left|\left|\mathbf{X_{NEO}^E}\right|\right| \\ \theta_0 &= \theta_{NEO} \\ \hat{r}_0 &= \left(\hat{\mathbf{r}} \bullet \mathbf{V_{NEO}^E}\right) \\ \hat{\theta}_0 &= \sqrt{\frac{\mu_{sun}}{a_{NEO}^3}}\,\frac{[1 + e_{NEO}\,\cos\theta_{NEO}]^2}{\sqrt{\left(1 - e_{NEO}^2\right)^3}} \end{cases} \tag{2.26}$$

Then, it is possible to compute the initial state of the impactor with Eq. 2.27; firstly, from the Hill's frame axes, the rotation matrix from ecliptic frame to Hill frame $\mathbf{A_{E/H}}$ is computed with Eq. 2.16. This matrix pre-multiplies the difference between the positions and velocities of impactor and NEO in the

heliocentric frame so that the obtained vector is rotated in the Hill's frame. In the case of the relative velocity $\dot{\boldsymbol{\rho}}_0$, the velocity component due to the rotation of the Hill's reference frame is added.

$$\begin{cases} \boldsymbol{\rho}_0 &= \mathbf{A_{E/H}} \left( \mathbf{X^E_{Imp}} - \mathbf{X^E_{NEO}} \right) \\ \dot{\boldsymbol{\rho}}_0 &= \mathbf{A_{E/H}} \left( \mathbf{V^E_{Imp}} - \mathbf{V^E_{NEO}} \right) - \begin{bmatrix} 0 \\ 0 \\ \dot{\theta}_0 \end{bmatrix} \times \boldsymbol{\rho}_0 \end{cases} \tag{2.27}$$

Finally, it is necessary also to compute the quaternion that describes the orientation of the spacecraft in Hill's frame. Recalling that the camera is mounted along the negative z axis of the body frame of the spacecraft, the aim is to have the negative z axis pointing towards the asteroid. Therefore, the rotation between the body axis [0 0 1] and the vector $\boldsymbol{\rho_0}$ is computed. The angle $\lambda$ between the two vectors and their normalised vectorial product $\hat{\mathbf{s}}$ are computed.Hence, the quaternion $\mathbf{q_{B/H}}$ that describes the rotation from body frame to Hill frame is:

$$\mathbf{q_{B/H}} = \left[ cos\left(\frac{\lambda}{2}\right) \, , \, sin\left(\frac{\lambda}{2}\right) \hat{\mathbf{s}} \right]$$

Then, inverting Eq. 2.17, it is possible to derive the quaternion $\mathbf{q_{H/E}}$ describing the rotation from Hill's frame to inertial frame. With these two quaternions, the initial quaternion describing the orientation of the spacecraft is computed with Eq. 2.28, through the quaternion multiplication.

$$\mathbf{q_0} = \mathbf{q_{B/H}} \times \mathbf{q_{H/E}} \tag{2.28}$$

#### 2.4.2.2.2 Sensors

Concerning the sensor part, since it is retained only the translational dynamics, the only sensor active is the navigation camera. At an acquisition rate of 20 seconds, the image that the camera will generate is obtained through Blender® in which is already loaded the 3D model of the asteroid. The scale factors, the relative position of spacecraft and NEO and also the orientation of the camera and the NEO are passed to Blender. Then from the focal length and resolution of the camera, Blender returns a black and white image.

Since in this thesis, the navigation will start at the spot time, that is when the camera sees the NEO only as a bright point in the sky, it is computationally inefficient to use Blender from the beginning, because the image returned will be dark with one pixel illuminated. Therefore, it is decided to generate a synthetic measurement of the position of the asteroid until the the size of the asteroid in the image becomes greater that 1 pixel.

The position of the asteroid in the camera expressed as azimuth and elevation angles is computed taking the state of the spacecraft that describes its relative position in the Hill's frame and rotating it in the body frame of the spacecraft. This vector already contains the information about azimuth and elevation angles; in fact those angles are computed in equation 2.29 and represented in Figure 2.8. The superscript B stands for "rotated in body frame", while the subscripts x, y, z, indicate the three components of the vector.

$$\begin{bmatrix} \gamma \\ \phi \end{bmatrix} = \arctan\left( \frac{1}{\rho^B_z} \begin{bmatrix} -\rho^B_x \\ \rho^B_y \end{bmatrix} \right) \tag{2.29}$$

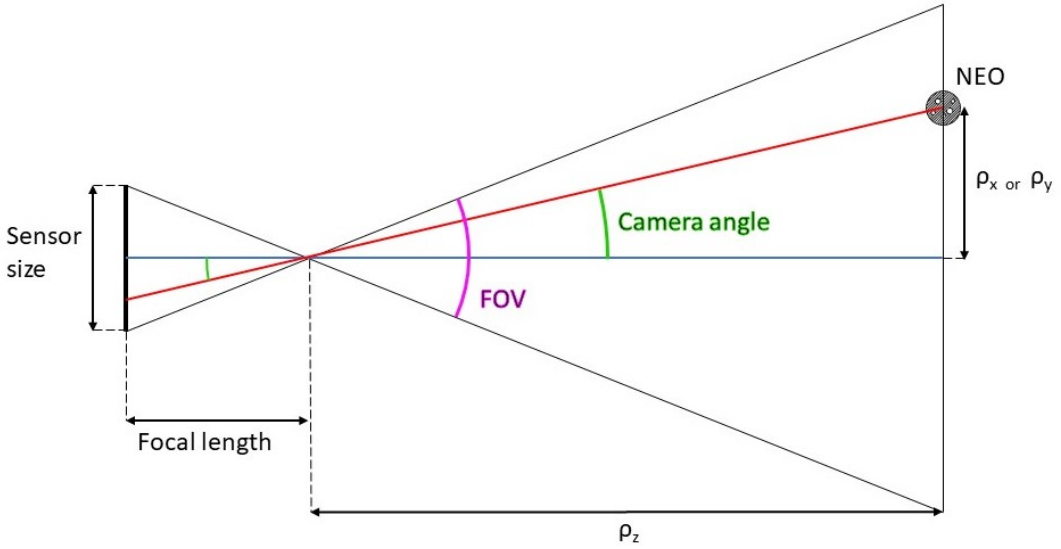


**Figure 2.8:** Graphical representation of azimuth and elevation angles.

#### 2.4.2.2.3 Extended Kalman Filter

The filter used in the model is the extended Kalman filter (EKF); it is a continuous-discrete filter, because the propagation of the estimated state is done continuously integrating in time differential equations, while the update of the state happens only when a new measurement from the sensor is available.

In this model it is represented only the translation dynamic of the spacecraft; therefore, the state of the spacecraft is:

$$\mathbf{x} = \begin{bmatrix} \boldsymbol{\rho} \\ \dot{\boldsymbol{\rho}} \end{bmatrix} \tag{2.30}$$

where $\rho$ and $\dot{\rho}$ are respectively the relative position and velocity of the spacecraft with respect to the asteroid in Hill's frame. The state space equations are:

$$\begin{cases} \dot{\mathbf{x}}(t) = \mathbf{f}(\mathbf{x}(t)) + \mathbf{u}(t) \\ \mathbf{y}(t) = \mathbf{h}(\mathbf{x}(t), t) + \mathbf{n}(t) \end{cases} \tag{2.31}$$

where **f** represents the equations of motion of the spacecraft, **u** is the control action of the spacecraft (the acceleration along the three axes), **y** is the measurement of the sensor that depends on the state through the equations **h**, and **n** is the noise of the measure.

Then the filter needs also the linearized equations in order to perform the update of the state [37]:

$$\begin{cases} \dot{\mathbf{x}}(t) = \mathbf{F}\,\mathbf{x}(t) + \mathbf{u}(t) \\ \mathbf{y}(t) = \mathbf{H}(t)\,\mathbf{x}(t) + \mathbf{n}(t) \end{cases} \tag{2.32}$$

with **F** and **H** being the Jacobian matrices already derived by Purpura [1].

$$\mathbf{F} = \left.\frac{\partial \mathbf{f}}{\partial \mathbf{x}}\right|_x \qquad \mathbf{H} = \left.\frac{\partial \mathbf{h}}{\partial \mathbf{x}}\right|_x \tag{2.33}$$

With these matrices, when a new measurement is available, it is possible to compute the gain matrix with equation 2.34. $\mathbf{P}^-$ and **R** are respectively the covariance matrix of the estimated state

before the new measurement and the covariance matrix of the noise **n**. Then, it is possible to update the estimation with eq. 2.35.

$$\mathbf{K} = \mathbf{P}^{-}\mathbf{H}^{\mathbf{T}}\left(\mathbf{H}\mathbf{P}^{-}\mathbf{H}^{\mathbf{T}} + \mathbf{R}\right) \tag{2.34}$$

$$\begin{cases} \hat{\mathbf{x}}^{+} & = \hat{\mathbf{x}}^{-} + \mathbf{K}\left(\mathbf{y} - \mathbf{H}\hat{\mathbf{x}}^{-}\right) \\ \mathbf{P}^{+} & = (\mathbf{I} - \mathbf{K}\mathbf{H})\,\mathbf{P}^{-} \end{cases} \tag{2.35}$$

Finally, the estimated state and the covariance matrix are propagated until a new measurement is available with eq. 2.36.

$$\begin{cases} \dot{\hat{\mathbf{x}}}(t) & = \mathbf{f}(\hat{\mathbf{x}}(t), t) + \mathbf{u}(t) \\ \dot{\mathbf{P}}(t) & = \mathbf{F}(t)\mathbf{P}(t) + \mathbf{P}(t)\mathbf{F}^{\mathbf{T}}(t) \end{cases} \tag{2.36}$$

#### 2.4.2.2.4 Control method

The control strategy is similar to the one of a missile that is programmed to hit a target in motion. In this case the target can not perform any manoeuvre; only the disturbances, like the solar radiation pressure, can change the trajectory of the asteroid but are neglected.
The control is based on the estimation of the state, that is composed by relative distance $\rho$ and relative velocity $\dot{\rho}$ of the spacecraft with respect to the asteroid. From the state, it is possible to compute the time for the spacecraft to hit the asteroid with no acceleration; it is computed from the projection of the distance from the asteroid along the velocity direction and divided by the modulus of the velocity:

$$t_{imp} = \frac{\boldsymbol{\rho} \cdot \hat{\boldsymbol{\rho}}}{||\dot{\boldsymbol{\rho}}||} \tag{2.37}$$

Then, are computed the perpendicular Zero Effort Miss ($ZEM_{\perp}$) and Zero Effort Velocity ($ZEV_{\perp}$). $ZEM_{\perp}$ is the distance between spacecraft and asteroid when the spacecraft misses the impact, that is when the relative velocity is perpendicular to the relative position vector. Instead, $ZEV_{\perp}$ is the velocity error, that is the velocity component normal to the relative distance. These errors are depicted in Figure 2.38 and are computed following Eq. 2.38.

$$\begin{cases} ZEM_{\perp} & = (\boldsymbol{\rho} \cdot \hat{\boldsymbol{\rho}})\hat{\boldsymbol{\rho}} - \boldsymbol{\rho} \\ ZEV_{\perp} & = (\dot{\boldsymbol{\rho}} \cdot \boldsymbol{\rho})\hat{\boldsymbol{\rho}} - \hat{\boldsymbol{\rho}} \end{cases} \tag{2.38}$$

Now, it is possible to compute the control acceleration:

$$\mathbf{u}(t) = \frac{6}{t_{imp}^{2}} ZEM_{\perp} - \frac{2}{t_{imp}} ZEV_{\perp} \tag{2.39}$$

However, the control algorithm is active only when the filter has obtained a good estimation of the position of the target. From the covariance matrix it is extracted the covariances of the lateral positions with respect to the asteroid. When these values go below 3 the algorithm enables the thrusters. This is an arbitrary limit that it will be tested in the optimisation process.

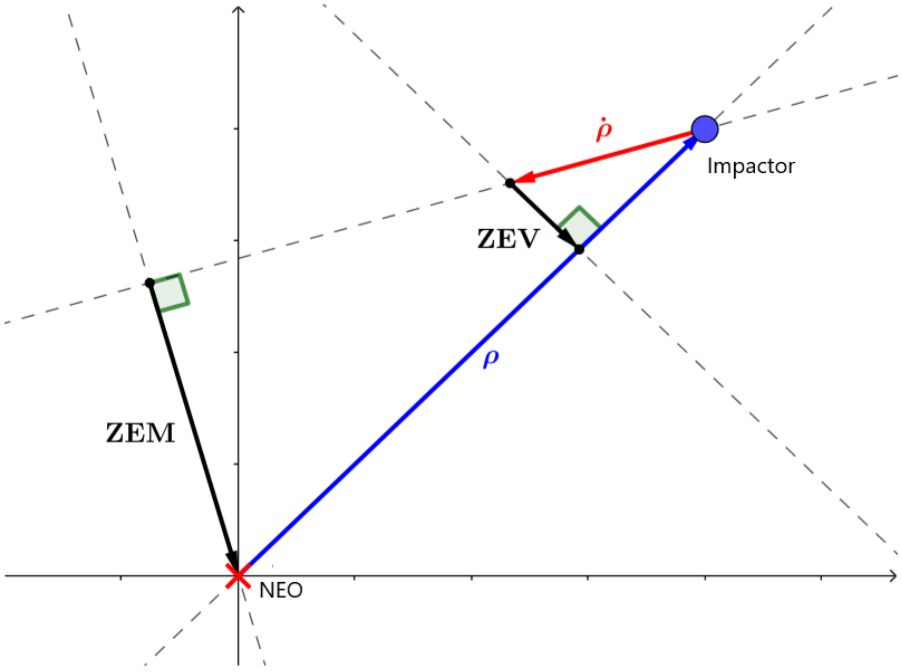


**Figure 2.9:** $ZEM_{\perp}$ and $ZEV_{\perp}$ from [1].

# 3 Asteroid impact model

This chapter presents the model of the impact with the asteroid. In detail, the assumptions and the equations to compute the efficiency of the impact are covered; then, it is also explained the propagation of the asteroid's orbit after the deviation.

## 3.1 Assumptions

There are several studies that tried to model the impact between an asteroid and a impactor. This thesis takes as reference the works of Yanagisawa [28] [29], Scheeres [31] and Zhang [30]. Yanagisawa performed a campaign of experiments to understand the hypervelocity impacts on to different materials and obtain a correlation between the momentum transfer and the angle of impact with the asteroid. While, the works of Scheeres [31] and Zhang [30] approached the problem from an analytical point of view obtaining the mathematical expressions that rules this phenomena.

The assumptions that were made are:

- target asteroid is a homogeneous monolithic body and does not destroy in pieces due to the collision;
- target asteroid is an ellipsoid with semi-axes a, b, c;
- melt and vaporisation of the surface are ignored;
- the collision destroys the impactor and creates rounded crater;
- the impact angle $\theta$, that is the angle between relative velocity of the impactor and vector normal to the surface of the asteroid at impact point, is less than 60 degrees; this assumption is to ensure circular crater but it will be relaxed in order to compute the efficiency also in the cases where it is not satisfied.
- all ejecta generated in the collision escapes from asteroid gravitational field.

## 3.2 Impact efficiency

In order to compute the momentum transferred to the asteroid and the efficiency of the impact, it is necessary to define two reference systems represented in Figure 3.1.
The first is the frame XYZ, with origin in the center of mass of the asteroid, that corresponds with the center of the ellipsoid assuming even mass distribution, and aligned with the semi-axes. In this frame the asteroid has zero velocity.
The second reference system is the local frame xyz, with the impact point as origin and z axis directed as the normal to the surface; the x axis is contained in the plane generated by axis z and vector **r** that

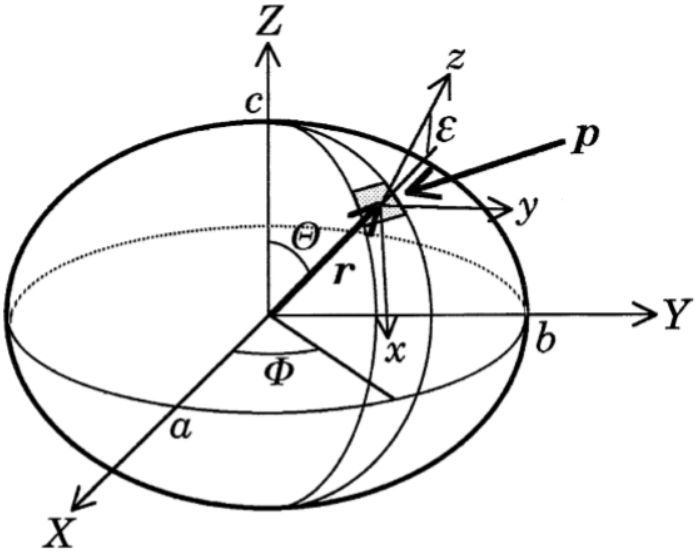


**Figure 3.1:** Ellipsoid reference frames from [30]: body frame XYZ and local frame xyz; **p** represents the impactor.

defines the impact point in XYZ frame. Then, the y axis is obtained with the right-hand rule.

The conservation of linear momentum equation is:

$$m\,\mathbf{v} = M'\,\mathbf{V}' + \mathbf{P_{ejecta}} \tag{3.1}$$

where m is the spacecraft mass, **v** is the spacecraft relative velocity with respect to the asteroid, M' and **V'** are respectively the post-impact mass and velocity of the asteroid and $\mathbf{P_{ejecta}}$ is the momentum of the ejecta.

The momentum of the ejecta can be hard to estimate with a mathematical model. In order to avoid the estimation of $\mathbf{P_{ejecta}}$, it is possible to define the normal and tangential multiplication factors as follow:

$$\eta = \frac{M'\,\mathbf{V'_n}}{m\,\mathbf{v_n}} \qquad \zeta = \frac{M'\,\mathbf{V'_t}}{m\,\mathbf{v_t}} \tag{3.2}$$

The subscripts n and t denote the local normal and local tangential components of the velocities. A campaign of tests was performed by Masahisa Y. and Sunao H. [29] to correlate the value of the multiplication factors to the impact angle. These tests were performed shooting nylon projectiles with a velocity between 0.76 and 4.4 km/s towards targets made of different materials like basalt, aluminum and mortar. The empirical correlations obtained are:

$$\begin{cases} \eta(\theta) & = 1 + \eta_0\,\cos^2\theta \\ \zeta(\theta) & = \zeta_0\,\cos^2\theta \end{cases} \tag{3.3}$$

The values of $\eta_0$ and $\zeta_0$ depend on the material of the target. For this thesis the values for basaltic asteroids are used, that are $\eta_0 = 1.52$ and $\zeta_0 = 0.409$. Figure 3.2 presents the value of $\eta$ and $\zeta$ as a function of $\theta$.

Remember that these correlations are valid for impact angles less than 60 degrees, but this constraint is relaxed and the equations are used also for greater angles. Now, it is possible to compute the variation of linear momentum of the asteroid:

$$\Delta\mathbf{P} = \eta\mathbf{P_n} + \zeta\mathbf{P_t} \tag{3.4}$$

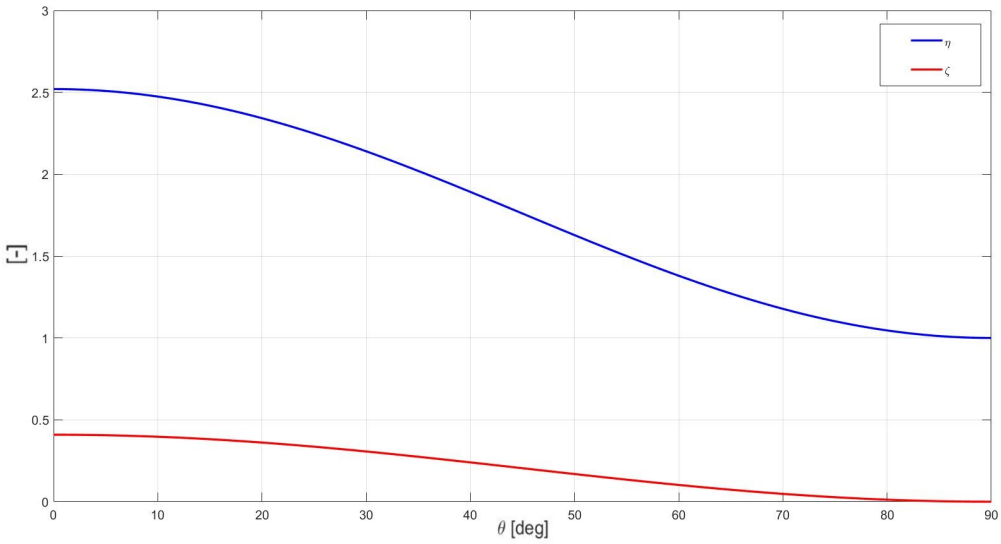


**Figure 3.2:** $\eta(\theta)$ and $\zeta(\theta)$ for basaltic asteroids.

with $\mathbf{P_n} = m\mathbf{v_n}$ and $\mathbf{P_t} = m\mathbf{v_t}$ be the normal and tangential component of the spacecraft momentum. Alongside, it is also possible to compute the variation of angular momentum with Eq. (3.5):

$$\Delta\mathbf{L} \approx r \times \Delta\mathbf{P} \tag{3.5}$$

This equation is not needed, but can be useful to model the variation in rotation velocity of the asteroid after the impact.

From Eq. 3.4, in order to compute the linear momentum variation of the asteroid, it is necessary to know the mass of the spacecraft at impact, its velocity in the asteroid local frame and the impact angle $\theta$. The navigation phase terminates when the last picture of the asteroid is taken; this means that it can stop between 20 and 1 seconds before the impact, because 20 seconds is the time between consecutive pictures. The useful outputs of the simulation are:

- $m_f$: final mass of the spacecraft;
- $\mathbf{x_H}$: estimated final state of the spacecraft, composed by relative position $\boldsymbol{\rho}_H$ and velocity $\dot{\boldsymbol{\rho}}_H$ in Hill's frame;
- $\mathbf{P_x}$: final covariance matrix of the state;
- $\mathbf{A_{H/E}}$: direct cosine matrix from inertial frame to Hill's frame;
- $\mathbf{q_{BE}}$: quaternion describing the orientation of the asteroid in inertial frame.

From $\mathbf{q_{BE}}$, it is possible to obtain the rotation matrix $\mathbf{A_{B/E}}$ and then, the relative position and velocity of the spacecraft with respect to the asteroid can be transported in the frame XYZ of the ellipsoid:

$$\begin{aligned} \boldsymbol{\rho}_B &= \mathbf{A_{B/E}}\,\mathbf{A_{H/E}}^{\top}\,\boldsymbol{\rho}_H \\ \dot{\boldsymbol{\rho}}_B &= \mathbf{A_{B/E}}\,\mathbf{A_{H/E}}^{\top}\,\dot{\boldsymbol{\rho}}_H \end{aligned} \tag{3.6}$$

Assuming that the spacecraft, from the last state until the impact, does not use the control action, it will follow a almost straight line. This straight line passes through the last position of the impactor $\boldsymbol{\rho}$

and it is parallel to the velocity of the impactor $\dot{\boldsymbol{\rho}}$. Therefore, it is possible to compute the impact point finding the intersection between the straight line and the ellipsoid that describes the asteroid. The intersections are found solving the set of equations:

$$\begin{aligned} &\text{Eq. of ellipsoid:} \quad \frac{x^2}{a^2}+\frac{y^2}{b^2}+\frac{z^2}{c^2}=1 \\ &\text{Eq. straight line:} \begin{cases} \frac{x-\rho_x}{\dot{\rho}_x}=\frac{y-\rho_y}{\dot{\rho}y} \\ \frac{z-\rho_z}{\dot{\rho}_z}=\frac{y-\rho_y}{\dot{\rho}y} \end{cases} \end{aligned} \tag{3.7}$$

Substituting the equation of the straight line in the equation of the ellipsoid, an equation of the second order is obtained in the form:

$$Ay^2+2By+C=0 \qquad \text{with:} \begin{cases} A=\frac{1}{a^2}\left(\frac{\dot{\rho}_x}{\dot{\rho}_y}\right)^2+\frac{1}{b^2}+\frac{1}{c^2}\left(\frac{\dot{\rho}_z}{\dot{\rho}_y}\right)^2 \\ B=\frac{\rho_x}{a^2}\left(\frac{\dot{\rho}_x}{\dot{\rho}_y}\right)+\frac{\rho_z}{c^2}\left(\frac{\dot{\rho}_z}{\dot{\rho}_y}\right)^2-\rho_y\left[\frac{1}{a^2}\left(\frac{\dot{\rho}_x}{\dot{\rho}_y}\right)^2+\frac{1}{c^2}\left(\frac{\dot{\rho}_z}{\dot{\rho}_y}\right)^2\right] \\ C=\left[\frac{1}{a}\left(\rho_x-\left(\frac{\dot{\rho}_x}{\dot{\rho}_y}\right)\rho_y\right)\right]^2+\left[\frac{1}{c}\left(\rho_z-\left(\frac{\dot{\rho}_z}{\dot{\rho}_y}\right)\rho_y\right)\right]^2-1 \end{cases} \tag{3.8}$$

If the determinant $Det=B^2-AC$ is less than zero means that the spacecraft misses the asteroid; if $Det=0$, the impact is tangent to the asteroid hence, $\theta=90$ deg; finally, if $Det>0$ there are two intersections and the impact point $\mathbf{X_i}$ is the nearest to $\boldsymbol{\rho_B}$.

Now, the normal vector to the surface of the asteroid at the impact point is computed:

$$\mathbf{n}=2\left[\frac{x_i}{a^2},\ \frac{y_i}{b^2},\ \frac{z_i}{c^2}\right] \tag{3.9}$$

Then, the impact angle is obtained, which allows to compute the multiplication factors $\eta$ and $\zeta$ using Eq. 3.10:

$$\theta=\arccos\left(\frac{\mathbf{n}\cdot\dot{\boldsymbol{\rho}}_{\boldsymbol{B}}}{\|\mathbf{n}\|\ \|\dot{\boldsymbol{\rho}}_{\boldsymbol{B}}\|}\right) \tag{3.10}$$

Through Eq. 3.4, the resulting linear momentum variation $\Delta\mathbf{P_{obt}}$ is obtained. Finally, it is possible to compute the efficiency of the impact, that is defined as the ratio between $\Delta\mathbf{P_{obt}}$ and a desired linear momentum variation, $\Delta\mathbf{P_{des}}$. This is evaluated with Eq. 3.4, imposing a perfect collision with the asteroid, therefore impact angle equal to 0 degrees, and taking the velocity at impact derived from the propagation with Keplerian motion of the nominal trajectory of the spacecraft. Then, the angle between $\Delta\mathbf{P_{obt}}$ and $\Delta\mathbf{P_{des}}$ is computed like in Eq. 3.10; it is called deviation angle $dev_{angle}$ and represents how much the momentum change obtained and the one desired are aligned.
At the end, the efficiency is defined as:

$$\epsilon=\frac{\|\Delta\mathbf{P_{obt}}\|\ \cos\left(dev_{angle}\right)}{\|\Delta\mathbf{P_{des}}\|} \tag{3.11}$$

Till now, the covariance matrix $\mathbf{P_x}$ is not used. This matrix is exploited to generate 1000 random positions and velocities of the spacecraft before impact starting from the estimated one so that 1000 efficiencies are computed and it is obtained a mean of the efficiencies $\mu_\epsilon$ and a variance $\sigma_\epsilon$. Since all the procedure has an analytical form, it is coded in vectorial form in Matlab, saving computation time, cause all the efficiencies are computed together.

In doing so, it is also possible to compute a probability to hit the asteroid, counting all the straight line trajectories that intersect the ellipsoid (the ones with $Det\geq 0$) and dividing by the total amount of points generated (in this case 1000):

$$P_{hit}=\frac{N_{impacts}}{1000} \tag{3.12}$$

## 3.3 ORBITAL PROPAGATION AFTER IMPACT

When the impactor hits the NEO, it imparts a momentum variation as computed in the previous section. The main purpose of the impactor is to deviate the asteroid's orbit such that the new MOID is larger than the unperturbed one. But, to compute the new MOID and then the radius of pericentre of the hyperbolic path of the NEO around the Earth with Eq. 2.5, it is necessary to compute the effects of the impact on the orbit. This computations are done assuming that the spacecraft follows its nominal trajectory and hits perfectly the NEO, so that it causes a variation in momentum equal to $\Delta\mathbf{P}_{\mathbf{des}}$.

The new orbit of the NEO can be considered proximal to the unperturbed orbit, therefore the variation of the position of the asteroid is written with the proximal motion equations expressed in Hill's following [8].

$$\begin{aligned}
\delta s_r &\approx \tfrac{r}{a}\delta a + \tfrac{ae\sin\Theta_{MOID}}{\sqrt{1-e^2}}\delta M - a\cos\Theta_{MOID}\delta e \\
\delta s_\theta &\approx \tfrac{r}{(1-e^2)^{\frac{3}{2}}}(1+e\cos\Theta_{MOID})^2\delta M + r\delta w + \\
&\quad + \tfrac{r\sin\Theta_{MOID}}{1-e^2}(2+e\cos\Theta_{MOID})\delta e + r\cos i\delta\Omega \\
\delta s_h &\approx r(\sin\Theta^*_{MOID}\delta i - \cos\Theta^*_{MOID}\sin i\delta\Omega)
\end{aligned} \tag{3.13}$$

where $\Theta_{MOID}$ is the true anomaly of the NEO at MOID and $\Theta^*_{MOID} = \Theta_{MOID} + w$ is the argument of latitude. Whereas, taking the velocity change of the NEO $\delta\mathbf{v} = [\delta v_t\ \delta v_n\ \delta v_h]$, the Gauss planetary equation are used to compute the variation of Keplerian parameters [8].

$$\begin{aligned}
\delta a &= \tfrac{2a^2 v}{\mu}\delta v_t \\
\delta e &= \tfrac{1}{v}\left[2(e+cos\Theta_i)\delta v_t - \tfrac{r}{a}\sin\Theta_i\delta v_n\right] \\
\delta i &= \tfrac{r\cos\Theta^*_i}{h}\delta v_h \\
\delta\Omega &= \tfrac{r\sin\Theta^*_i}{h\sin i}\delta v_h \\
\delta\omega &= \tfrac{1}{ev}\left[2\sin\Theta_i\delta v_t + (2e+\tfrac{r}{a}\cos\Theta_i)\delta v_n\right] - \tfrac{r\sin\Theta^*_i\cos i}{h\sin i}\delta v_h \\
\delta M &= -\tfrac{b}{eav}\left[2\left(1+\tfrac{e^2 r}{p}\right)\sin\Theta_i\delta v_t + \tfrac{r}{a}\cos\Theta_i\delta v_n\right] + \left(\sqrt{\tfrac{\mu}{a^3}} - \sqrt{\tfrac{\mu}{(a+\delta a)^3}}\right)(t_{MOID} - t_i)
\end{aligned} \tag{3.14}$$

with the subscript i standing for "impact". With this new orbit it is possible to compute the new radius of pericentre of the hyperbola around the Earth by means of Eq. 2.5.

# 4 Sensitivity analysis to camera features

Before starting the optimisation process, it is interesting to analyse the behaviour of the control algorithm in the simulation and the impact performances for varying camera features and asteroid dimension.

In detail, the parameters of interest of the camera are:

- the Focal Length of the camera (FL);
- the Resolution of the detector (Res), that is equal to the number of pixels in a row;
- the size of the detector ($\text{Sens}_{\text{size}}$), that for simplicity is considered a square.

Focal length and sensor size determine the Field Of View (FOV) of the system through the relation:

$$Sens_{size} = 2\ FL\ \tan\left(\frac{FOV}{2}\right) \tag{4.1}$$

With Eq. 4.1 the longer is the FL the smaller is the FOV and, maintaining the same sensor size and resolution, the camera can resolve an object from a larger distance. This can be useful in the final part of the navigation phase, when the asteroid occupies more than 1 pixel in the image and the algorithm that computes the centroid of the asteroid starts.

The three parameters are also linked by the equation that computes the size of the asteroid in the image measured in pixels:

$$\text{Ast-Image}_{px} = D_{ast}\frac{FL\ Res}{dist\ Sens_{size}} \tag{4.2}$$

where $D_{ast}$ is one diameter of the asteroid and $dist$ is the distance NEO to camera. Therefore, considering Eq. 4.2, also an increment in the resolution can improve the resolving power of the system; but, there is the limit of the size of the pixels that is:

$$Size_{px} = \frac{Sens_{size}}{Res} \tag{4.3}$$

Sensore size and resolution must generate a reasonable dimension of the pixel in order to be not too small to be constructed; a typical values for the size of a pixel is in the order of the micrometers.

In order to select a feasible camera, the results obtained with four existing cameras and two proposed by Purpura [1] are compared. The cameras are:

- The ECAM-C50: the camera proposed by C. Colombo et al. [5]. It is the one with the shortest focal length.
- The camera used in the NASA mission Deep Impact [35];

- The navigation camera of ESA Rosetta mission [36];
- The Long Range Reconnaissance Imager (LORRI) designed for the New Horizons that has the highest focal length [32];
- The first proposed camera that is like Rosetta's but with a higher resolution (CAM 1) [1];
- The second proposed camera that employs the smaller sensor of ECAM-C50 but maintains the focal length of Rosetta's (CAM 2) [1].

In the following table are reported the main characteristics of these cameras:

| | | C50 | D.I. | Ros. | LORRI | CAM 1 | CAM 2 |
|---|---|---|---|---|---|---|---|
| Focal length | [mm] | 12.6 | 2100 | 152.5 | 2630 | 152.5 | 152.5 |
| Resolution | [px] | 1944 | 1024 | 1024 | 1024 | 1944 | 1944 |
| Sensor size | [mm] | 4.2 | 22.0 | 13.3 | 13.3 | 13.3 | 4.2 |
| FOV | [deg] | 19 | 0.6 | 5 | 0.29 | 5 | 1.58 |

**Table 4.1:** Main parameters of the cameras.

## 4.1 CAMERA SELECTION

To compare the cameras, the spacecraft is inserted in a direct transfer orbit that is taken as test case. This trajectory, presented in detail in section 5.1.1, is the result of a Lambert problem between a departure condition from Earth and a nominal impact point with the NEO. During the whole trajectory the spacecraft is in the so called coast phase explained in Section 2.4.2.1, until the asteroid becomes visible to the camera as a lighted pixel. Knowing the time at which this condition occurs using the method of Section 2.4.2.1.1, the initial position and velocity of both spacecraft and asteroid for the navigation phase are derived.

These initial conditions can be set in the Simulink model together with the dimension of the asteroid and the camera features. The NEOs are considered to be spheres with a diameter of 500, 200, 100 and 50 m. Every camera is tested for each asteroid dimension, for a total of 24 runs. The aim is to analyse how the probability of impact with the NEOs changes with different cameras; then are also compared the maximum lateral error of the spacecraft and the behaviour of the control action for the different optics.

From the output of the simulation, the probability of impact with the NEO can be reconstructed exploiting the method presented in section 3.2. Figure 4.1 reports different probabilities of impact for all the cameras. It is possible to see that for asteroids with a mean diameter grater than 500 m all the cameras hit the asteroid 100% of the time. Then the probability decreases to around 70% for 200 m and 30% for 100 m. Finally, it is only 8% for the 50 m asteroid. The maximum spread of the probabilities is for the asteroid of 200 meters in diameter and it is highlighted in Figure 4.2; however, the spread remains below 3%, suggesting that the behaviour of the spacecraft is not so sensitive to the on-board optical equipment.

From Eq. 4.2, that relates the dimension in pixel of the asteroid in the image to its real dimensions and the camera features, it is possible to make a first comparison of the resolving power of the cameras. Figure 4.3 shows the dimension of the asteroid in the image as a function of the distance for all the cameras considered; the solid line is for the 500 m asteroid while the dashed line for the 50 m asteroid

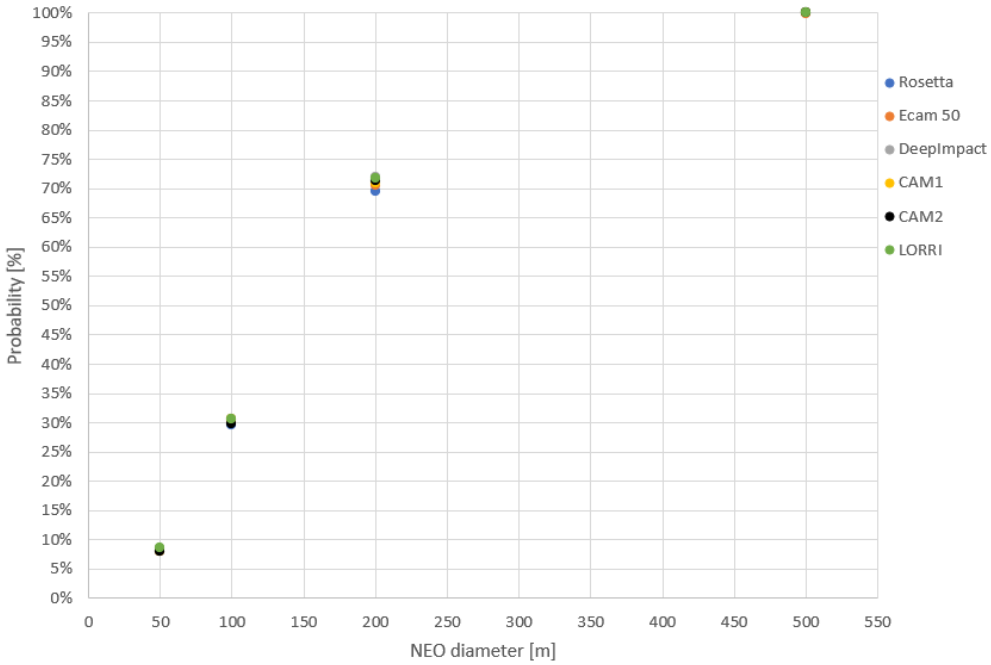


**Figure 4.1:** Probability of impact for different asteroid's diameters and cameras.

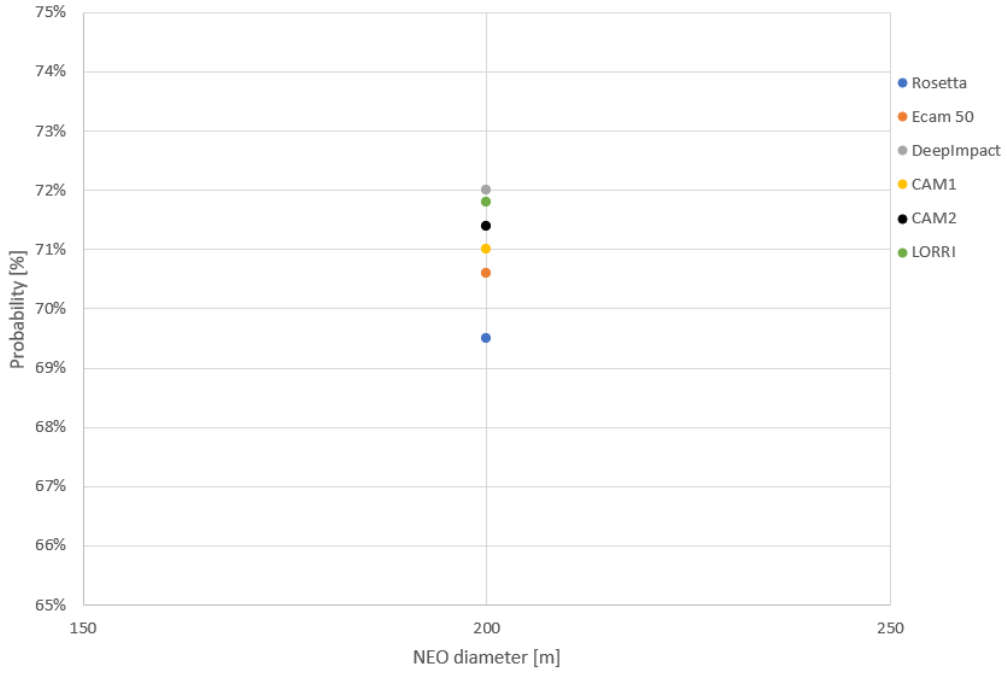


**Figure 4.2:** Probability of impact for 200 m asteroid

and in red is highlighted the condition $Ast_{size} = 1px$. The best camera in terms of resolving power is the LORRI, followed by D.I. and CAM 2, because they are the cameras with the smallest field of view; then, CAM 1, Ros., and ECAM have the smallest resolving power. For the 500 m asteroid, if the distance from spacecraft to NEO is above 100000 km, none of the cameras can resolve the target. This value drops of a factor 10 in the case of the 50 m asteroid since the dimension in the image is directly proportional to the real size of the NEO.

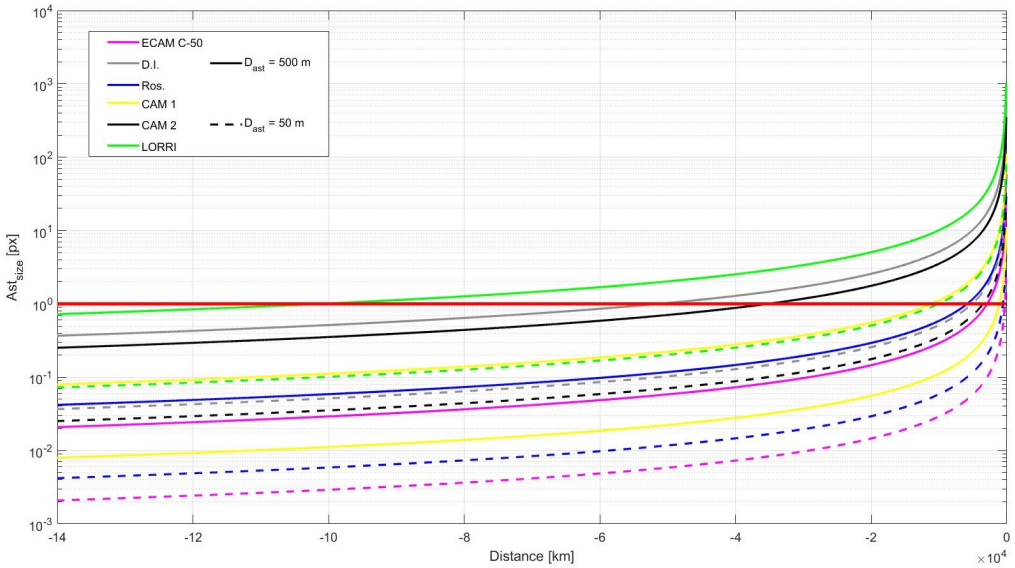


**Figure 4.3:** Dimension of asteroids in pixel for all the cameras and for NEO with diameter of 500 and 50 m as a function of the distance from the spacecraft

The time at which the asteroid dimension in the image becomes greater than 1 pixel depends on the relative velocity between NEO and spacecraft and therefore on the trajectory the spacecraft follows. From that instant, the first picture of the asteroid is generated through Blender and the image analyzer starts. From the simulations, the times of the first image are different for all the cameras and are directly proportional to the dimension of the asteroid. Figure 4.4 shows that linear trend; the cameras with the higher resolving power can see the target earlier. For example the LORRI can resolve the 500 m NEO 28940 seconds before impact and the 50 m NEO 2880 seconds before. On the other hand, the ECAM C-50 resolves the asteroid of 50 m, only 60 seconds before impact, hence it shots only 3 pictures of the NEO during the hole mission.

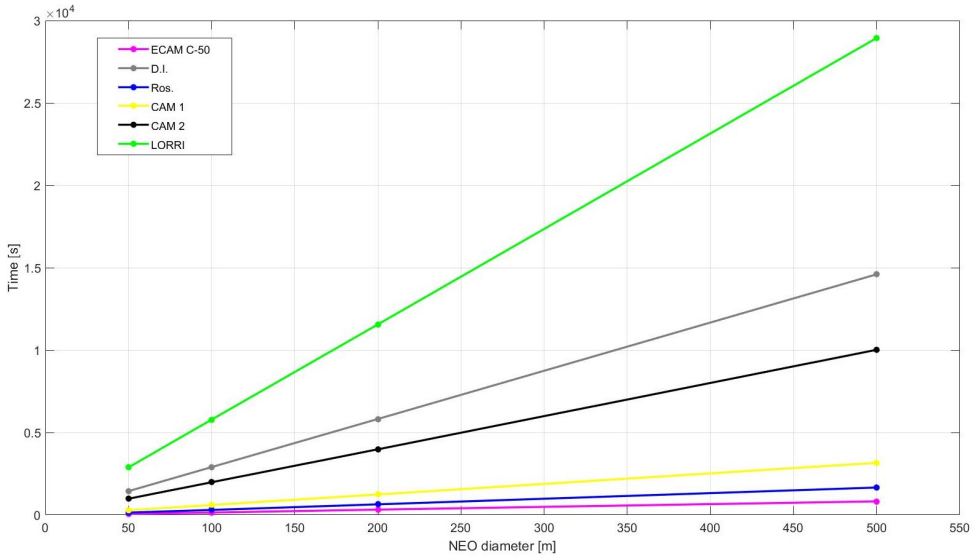


**Figure 4.4:** Time of first NEO image before impact as a function of the NEO diameter.

However, the probability of impact with the NEO is very similar for each camera and does not seem to depend on the resolving power. This is because the control action starts before the target is resolved in the image. In fact, the control is enabled when a good estimation of the position of the asteroid is obtained; the estimation depends on the camera features but, since most of the measurements are collected when the asteroid is less than 1 pixel in the image and all the cameras mounted have the same aperture of the optic, the differences between them are smoothed out. Therefore, the control time is common to every camera and it is about 46000 seconds for the 500 m asteroid and 18000 seconds for the 50 m asteroid.

Figures 4.5 and 4.6 show the evolution of the ZEM during the run of the spacecraft with the LORRI camera mounted and colliding with the 500 m asteroid. Initially, the ZEM raises because the distance from the target is too big and the estimation of the position of the asteroid is poor. As the spacecraft approaches the target the ZEM decreases because the spacecraft is in route of collision with the NEO; however the control action is still needed to correct the initial position and velocity errors. Then, in Figure 4.6 that is a zoom in the last part of the simulation, is possible to appreciate how the control makes the ZEM to converge to zero; when the ZEM curve crosses the yellow vertical line, that corresponds to the time at which the control is enabled, there is a sudden change of inclination, proving that the spacecraft is capable of correct the trajectory to hit the asteroid.

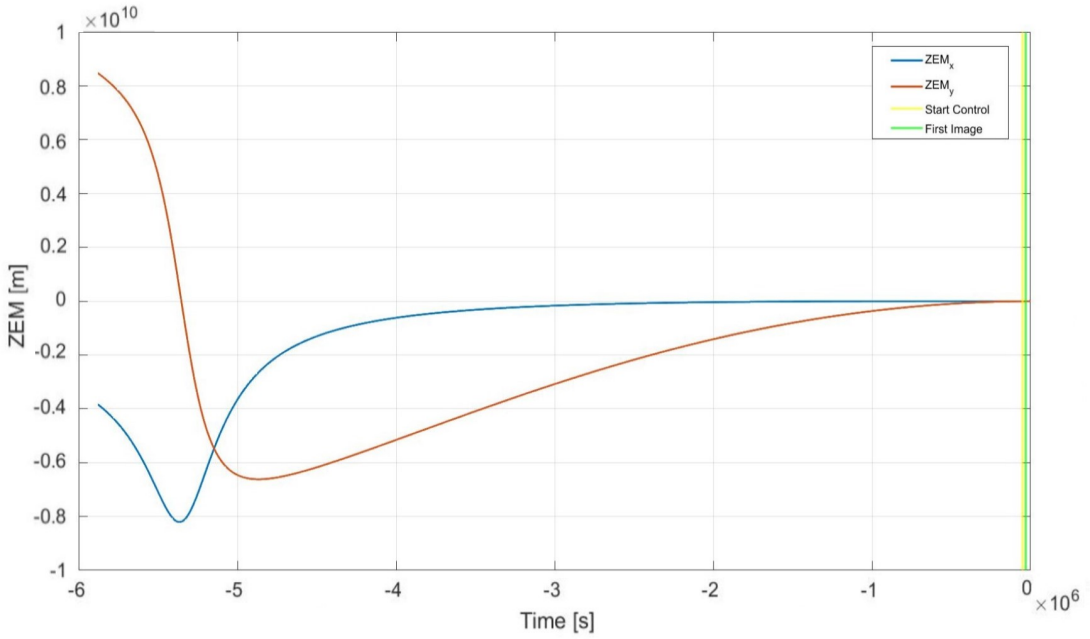


**Figure 4.5:** Zero Effort Miss for LORRI camera and 500 m asteroid during the simulation.

Since all the cameras have the same behaviour and lead to similar results, the selection of the camera features seems not so important. However, taking as selection criteria the probability of impact represented in Figure 4.2, it is chosen the CAM 1 because is the one that represents better all the cameras. Otherwise, if the aim is to maximise the performances, the LORRI camera can be selected even if the improvements are small.

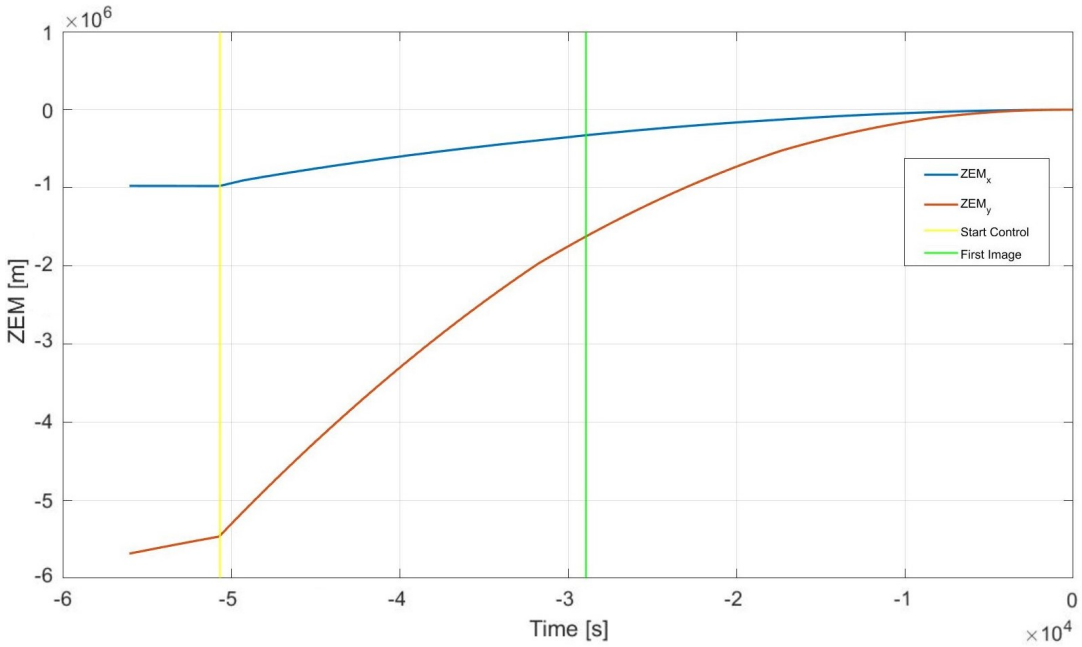


**Figure 4.6:** Zoom of Figure 4.5 in the control region.

# 5 Spacecraft trajectory optimisation

In the final part of this thesis, firstly the nominal trajectory of the spacecraft is optimised. Three different approaches will be presented for the nominal trajectory: a direct transfer from Earth's orbit to the NEO, a direct transfer with a planned deep space manoeuvre and a multi-revolution transfer. To find the trajectory, it is performed a global optimisation of the decision variables that will be presented in each section.

Then, the local optimisation follows; there a scenario is tested where a new estimate of the Keplerian parameters of the NEO are provided by ground stations observations and the spacecraft has to perform a deep space manoeuvre to correct its orbit; furthermore, inside the optimisation the simulation of the navigation is also inserted, so that the efficiency of the impact with the asteroid can be optimised.

The optimisation problem is typically a minimisation problem that can be written in the form:

$$\min J(x) \quad \text{such that}: \begin{cases} c(x) \leq & 0 \\ c_{eq}(x) = & 0 \\ A\,x \leq & b \\ A_{eq}\,x = & b_{eq} \\ lb \leq & x \leq ub \end{cases} \tag{5.1}$$

In this system of equations, $x$ represents the decision variables, that are the parameters that the algorithm is allowed to modify in order to minimise the fitness function $J(x)$ (sometimes called also objective function). Then, there are the constraints on the decision variables that are divided in: $c(x)$ and $c_{eq}(x)$ that are respectively the non-linear inequality and non-linear equality functions; $A$, $b$, $A_{eq}$, $b_{eq}$ are instead the linear inequality and equality constraint. If $x$ is a column vector [n × 1] and $p$ is the number of linear constraints, then $A$ is a matrix [p × n] and $b$ is a column vector [p × 1]. Finally $lb$ and $ub$ are the lower and upper boundary in which the decision vary. To perform the optimisations the built-in MATLAB® functions ga (genetic algorithm) and fmincon are used.

Genetic Algorithm is a method to solve optimisation problems based on the process of natural selection [39]. At the beginning of the optimisation, a population of individuals with different decision variables consistent with the boundaries is generated randomly or it can be passed by the user. For each individual is computed the value of the fitness function; these raw values are then scaled to obtain a score for each individual. The individuals with the best score are selected to be the parents of the next population; this is done via a stochastic uniform selection, in which the number of times an individual reproduces, is proportional to its score. Figure 5.1 illustrates the generation of the new individuals. The two individuals with the best score are the Elite children and can survive to the next generation; then, from the parents, two other kind of children are generated. 80% of them are crossover children that are formed by combining the genes (the value of the decision variables) of two parents; the remainder are

mutation children that are consequence of a random mutation of a single parent.
The algorithm stops when reaches the maximum number of generations set by the user or when the change in the fitness function is less than a tolerance value, that for all the cases is left equal to the default value of $10^{-6}$. The convergence of this algorithm is not proven, but it is suited to search for global minimum because can span different basins of attraction.

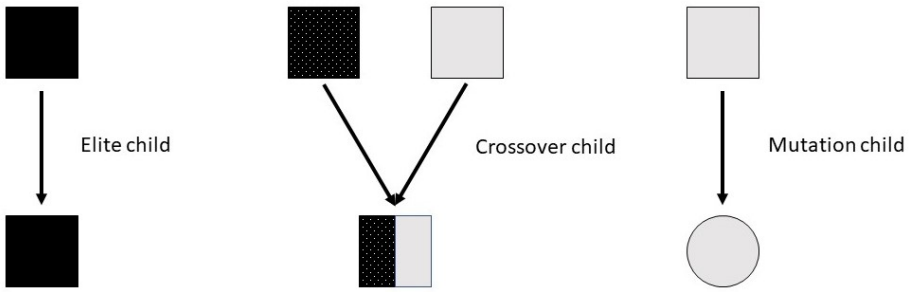


**Figure 5.1:** Children generation in the genetic algorithm.

The other optimisation toll used is fmincon that has a proven quadratic convergence to local optima and it is suited to refine or search for a minimum near a guess solution. This method, needs the user to provide a initial point to start the optimisation; in this thesis, the guess solution is provided by the output of the ga. Then, the interior-point algorithm takes several steps from the guess solution evaluating each time the fitness function; if the function around the initial guess point is convex the algorithm should remain in this basin and refine the solution. As the ga, fmincon stops when the variation in the objective function is less than $10^{-6}$.

## 5.1 GLOBAL OPTIMISATION

The global optimisation is performed through the genetic algorithm. The population is composed by 1000 individuals for all the analysed cases; if not differently expressed, the initial population is randomly generated by the algorithm. The aim of this optimisation is to find the optimal nominal trajectory to obtain the maximum deviation of the asteroid orbit.

Therefore, as fitness function for all cases, it is used the difference between the radius of pericentre of the hyperbolic trajectory of the NEO around the Earth, before and after impact [2]:

$$J = -(r_p - r_{p_0}) \tag{5.2}$$

Since the goal is to maximise the radius of pericentre, the minus sign is added because the optimiser minimises the fitness function. Once the genetic algorithm terminates, it gives as output the minimum computed value of the optimisation function and its corresponding decision variables. These variables are used as starting solution for the fmincon function to refine the result obtained; obviously, fmincon minimises the same fitness function J of Eq. 5.2.

Finally, all the optimisations have in common some parameters:

- the time at which the NEO is at MOID, $t_{MOID}$;
- the warning time, that is how much before the impact time the NEO is spotted by the ground observatories. From [8], a reasonable value is $t_{warning} = 10$ years. Hence, the time at which the observatories spot the asteroid is $t_{discovery} = t_{MOID} - t_{warning}$;

- the parameters of the spacecraft presented in section 2.4.1.

In this thesis the approach in [2], [5] is followed; therefore, the studied case are:

1. the direct transfer from Earth to NEO;
2. the direct transfer with a DSM;
3. the one-revolution transfer from Earth to NEO.

### 5.1.1 Direct transfer

In the direct transfer case the spacecraft leaves Earth's gravitational field with an excess velocity provided by the launcher that can not be higher than 3 km/s. Moreover, the launcher puts the spacecraft already in a collision trajectory with the asteroid. To compute this trajectory, it is necessary to know the departure time from Earth and the time of flight from departure to impact. Therefore, $\alpha$ and $TOF$ are selected as decision variables for this case.

$TOF$ stands for Time Of Flight, and it is the time the spacecraft takes to reach the asteroid counting from the departure. Whereas, $\alpha$ is a percentage, hence can assume values from 0 to 1. It is used to compute the departure time ($t_0$) from the Earth following [2].

$$t_0 = t_{discovery} + (t_{warning} - TOF)\alpha \tag{5.3}$$

In the fitness function, the departure position is computed from $t_0$ and the Earth's ephemerides; then, the impact time is:

$$t_{imp} = t_0 + TOF \tag{5.4}$$

With $t_{imp}$ and the ephemerides of the NEO, the position of the asteroid at impact is computed and then it is solved the Lambert problem between the NEO position at impact and Earth's position at departure, imposing the selected time of flight. The outputs are the departure velocity and impact velocity of the spacecraft. From the relative velocity between NEO and spacecraft at impact, it is computed the momentum change of the asteroid; finally, it is computed the new orbit with the Gauss planetary equations like in Section 3.3, then the new MOID and the radius of pericenter of the hyperbola.

Returning to the decision variables, a value of $\alpha$ near zero, means that the spacecraft departs from Earth as soon as the NEO is spotted; instead when $\alpha$ is near one the spacecraft departs at the last moment. Values of $\alpha$ close to zero are expected because the earlier the impact with the asteroid, the higher the deviation at $t_{MOID}$.

Whereas, the value that can assume the time of flight goes from 30 days to three times the greatest orbital period among the NEO and the Earth ($T_{max}$).

The boundaries for the values of $\alpha$ and $TOF$ are summarized in Table 5.1.

| | $\alpha$ [-] | TOF [days] |
|---|---|---|
| Boundaries | [0 1] | [30 3*$T_{max}$] |

**Table 5.1:** Decision variables lower and upper bounds for direct transfer

### 5.1.2 Direct transfer with DSM

In the second case, it is decided to perform a deep space manoeuvre (DSM) before the impact with the asteroid. This adds more degrees of freedom to the problem. More precisely instead of 2 decision variables, now 6 decision variables are available that are:

- $\alpha$: defined as in Section 5.1.1, it is necessary to compute the departure time with Eq. 5.3;
- $\beta$: it is a percentage of the TOF that determines where the DSM is performed; following Figure 5.2, after the departure from Earth, the spacecraft follows its trajectory for $\beta TOF$ days and performs the DSM;
- $TOF$: as in the previous section is the time of flight from departure to impact;
- $||\boldsymbol{\Delta V_0}||$: it is the norm of the excess velocity that is provided by the launcher;
- $\psi_{\Delta V_0}$: it is the angle between the projection of the $\boldsymbol{\Delta V_0}$ vector on the ecliptic plane and Earth's velocity (called in-plane angle);
- $\delta_{\Delta V_0}$: it is the angle between the $\boldsymbol{\Delta V_0}$ vector and the normal to the ecliptic plane (called out-of-plane angle).

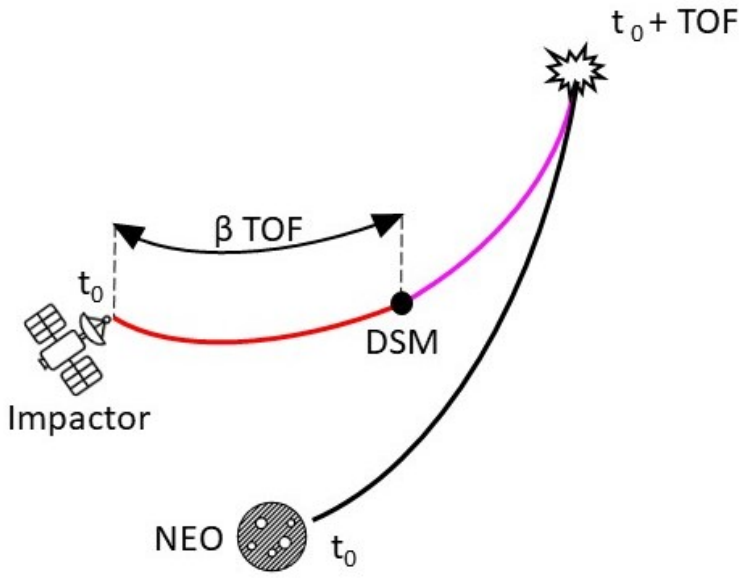


**Figure 5.2:** Graphical representation of the spacecraft trajectory from departure to impact

With the position at departure computed from $\alpha$ like in the direct transfer case and the norm of $||\boldsymbol{\Delta V_0}||$, together with its angles $\psi$ and $\delta$, it is possible to compute the state of the spacecraft at departure. In fact the position coincides with Earth's position, while its velocity is the velocity of the Earth plus the $\boldsymbol{\Delta V_0}$ vector expressed in heliocentric frame.

In this case the spacecraft is not in route of collision with the asteroid, because the DSM corrects the orbit. The time at which the spacecraft performs the DSM is computed through the variable $\beta$:

$$t_{DSM} = t_0 + \beta\ TOF \tag{5.5}$$

Therefore, from position and velocity of the spacecraft, its trajectory is propagated in time for $\beta TOF$ seconds; the new position and velocity obtained, are the condition of the spacecraft when it performs the burn for the DSM. The difference in velocity to be imparted to the spacecraft is computed solving the Lambert problem between position of the spacecraft at DSM and position of the asteroid at impact. The NEO position and velocity at impact are obtained again propagating its position and velocity at $t_0$ for an amount of time equal to the $TOF$.

In Table 5.2 are presented the lower and upper bounds for the decision variables.

| | $\alpha$ [-] | $\beta$ [-] | TOF [days] | $\|\|\mathbf{\Delta V_0}\|\| \left[\frac{km}{s}\right]$ | $\psi_{\Delta V_0}[rad]$ | $\delta_{\Delta V_0}[rad]$ |
|---|---|---|---|---|---|---|
| Boundaries | [0 1] | [0 0.9] | [30 $3^*T_{max}$] | [0 3] | $[-\pi \quad \pi]$ | $[-\frac{\pi}{2} \quad \frac{\pi}{2}]$ |

**Table 5.2:** Decision variables lower and upper bounds for direct transfer with DSM

The maximum value of $\beta$ is set to 0.9 because the final part of the trajectory will be occupied by the approach phase, including continuous navigation and control; therefore, in the last 10% of the nominal trajectory no manoeuvre can be inserted. The maximum value of the $||\mathbf{\Delta V_0}||$ was already set to 3 km/s in Section 2.4.1, while the minimum and maximum value of $\psi_{\Delta V_0}$ and $\delta_{\Delta V_0}$ are set by construction.

Moreover, it is also necessary to limit the maximum ΔV that the spacecraft can provide with the DSM; the limit was computed in section 2.4.1, and it is around 3.5 km/s. This limit is set with a non-linear constraint function that, for each individual, computes the expected $\Delta V_{DSM}$ and checks whether its value is higher than 3.5 km/s.

For this particular case it is also decided to control part of the initial population generated by the genetic algorithm, because, after trying several times to optimise these decision variables, sometimes the algorithm converges to points that were checked to not be the global minimum.
Therefore, 15% of the initial population is generated randomly by ga, but the remaining 85% is generated with guessed values. In particular conditions where $\alpha$ has always values between 0.025 and 0.2 are generated, because it is expected that the optimal condition is when the spacecraft departures from Earth as early as possible. Also for the $||\mathbf{\Delta V_0}||$ values between 2 and 3 are guessed, because since this change in velocity is provided by the launcher without affecting the mass of the spacecraft, the optimal solution will use as much as possible this "free" energy; in fact, using the propellant loaded on the spacecraft to perform the DSM would decrease the final mass of the spacecraft and, as a consequence, the linear momentum imparted to the asteroid.

### 5.1.3 Multi-revolution transfer

This last case for the global optimisation is very similar to the direct transfer. In fact, the decision variables are the same: $\alpha$ and $TOF$. But this time, it is imposed to the spacecraft to execute one entire orbit before hitting the asteroid.

The procedure is the same as in the direct transfer, but when solving the Lambert problem, instead of having only one solution, now two solutions are possible. From article [40] is extracted Figure 5.3 which shows that for a number of revolutions greater than 1, given a specific transfer time two solutions are possible that differ from the semi-major axis.

If one of the solution is not feasible because exceeds the limit of the initial $\Delta V_0$ of 3 km/s, it is selected the other. Instead, if both the trajectories respect the constraint on the excess velocity of the

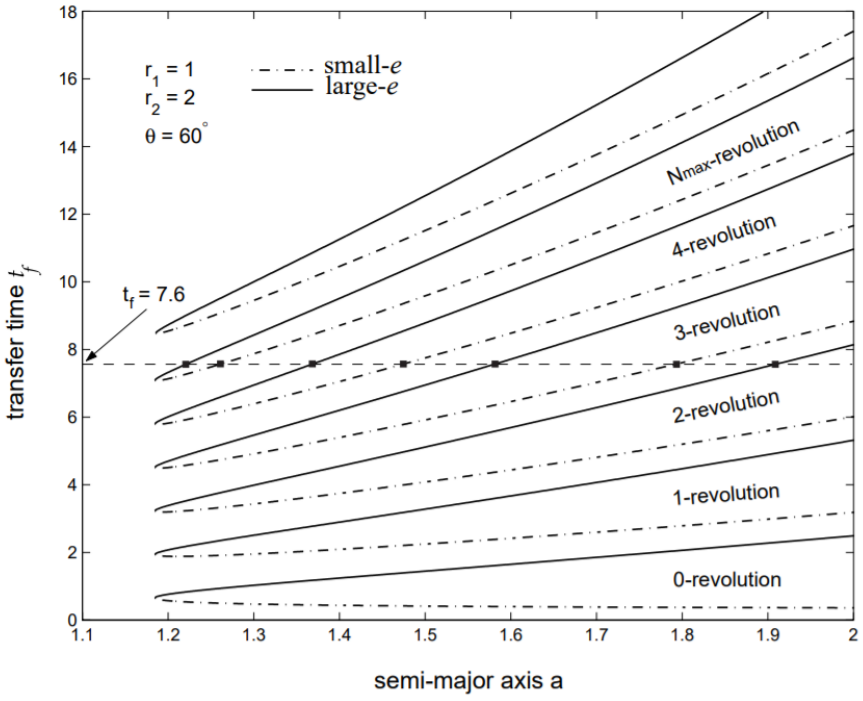


**Figure 5.3:** Semi-major axis of the transfer orbit depending on the transfer time from [40].

launch, the fitness function is computed in both cases and it is retained the trajectory that obtains the best score.

Lastly, the bounds for the time of flight are extended, since the spacecraft has to perform one entire orbit before impact and it is counted in the $TOF$. The maximum acceptable value of $TOF$ is changed to the minimum between the warning time and $8T_{max}$, where $T_{max}$ is the maximum orbital period among Earth and NEO. Table 5.3 reports the bounds of the decision variables.

| | $\alpha$ [-] | TOF [days] |
|---|---|---|
| Boundaries | [0 1] | [30 $\min(t_{warning}, 8T_{max})$] |

**Table 5.3:** Decision variables lower and upper boundaries for multi-revolution transfer

### 5.1.4 Results

In this section the results of the global optimisations are presented. It is important to notice that, these optimisations are independent on the dimension and so, mass of the target asteroid. In fact, whenever a trajectory is optimal, independently on the mass of the asteroid, it will cause the maximum deviation achievable; therefore, the optimal decision variables, which determine the spacecraft's trajectory, are very similar on varying NEO's dimensions. Due to the stochastic nature of the genetic algorithm, there can be small variations of the optimal decision variables between different runs because ga converges in a neighborhood of the optimal solution. Obviously, what is dependent on the mass of the asteroid is the value that the fitness function assumes at the optimal solution; it will be higher for small asteroids and lower for the larger ones.

#### 5.1.4.1 Direct transfer results

The optimal solution for the direct transfer case is identified by the values for the decision variables reported in Table 5.4.

| $\alpha_{opt}$ [-] | $TOF_{opt}$ [days] |
|---|---|
| 0.1215 | 461.5 |

**Table 5.4:** Optimal decision variables for direct transfer case

With these values, the departure date is on January 20, 2087, about 8 years before the MOID. As expected, the value of $\alpha$ is small, because the earlier the impact the greater the deviation at the MOID, because the deviation accumulates during each orbit of the NEO around the Sun.

The orbit obtained is depicted in Figure 5.4. The trajectory followed by the spacecraft is in red, while the orbit of Earth and asteroid are respectively painted in blue and black.

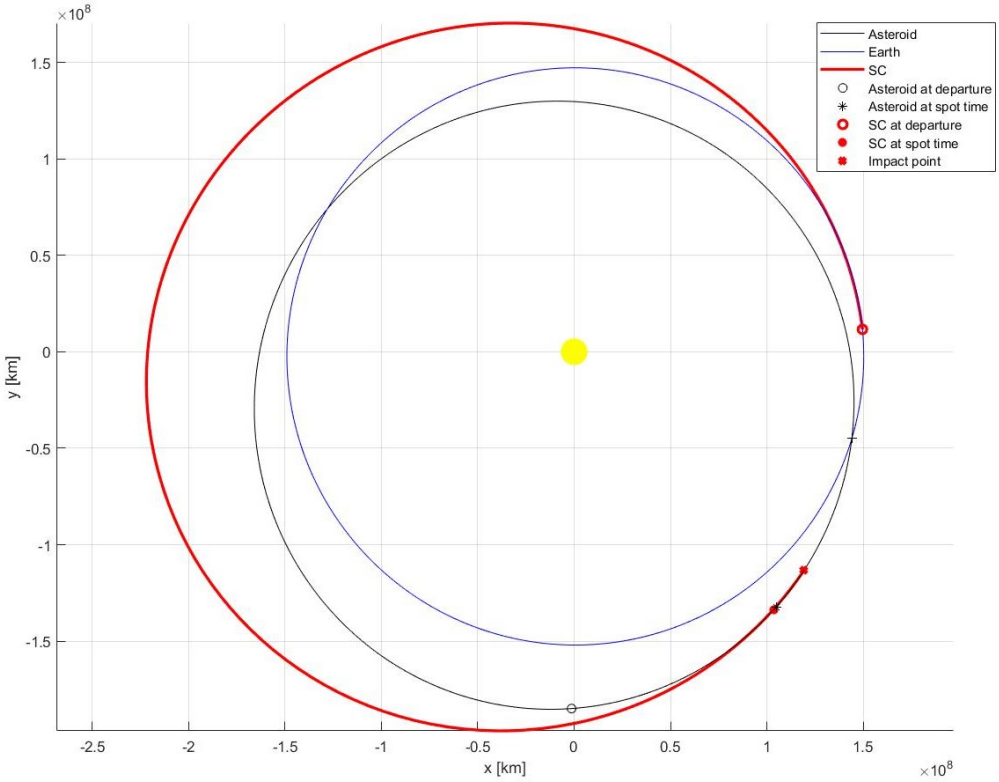


**Figure 5.4:** Direct transfer optimal trajectory

From the picture, it is evident that at the impact point the spacecraft's orbit and the asteroid's one are almost parallel; this is a result that was obtained from other studies like [5],[8]. The angle between spacecraft's velocity and asteroid's velocity at impact is less than 5 degrees. This means, that the Sun angle is almost 90 degrees, so half of the asteroid is illuminated, useful for the navigation and control.

Another important aspect is that the $\Delta V$ used for the launch is 3 km/s, that is the maximum available, and it is nearly parallel to the velocity of Earth at departure. These results confirms that the solution found is optimal, because a $\Delta V$ along the velocity vector is the most efficient way to

accelerate a spacecraft; moreover, the spacecraft takes advantage of all the excess velocity the launcher can provide. This orbit leads to a relative velocity of the spacecraft with respect to the NEO at impact around 2320 m/s.

Then, in Table 5.5, it is possible to analyse the values that the fitness function assumes with varying asteroid dimension.

| $D_{NEO}$ [m] | $J = -(r_p - r_{p_0})$ [km] |
|---|---|
| 50 | -10112 |
| 100 | -1203 |
| 200 | -150 |
| 500 | -10 |

**Table 5.5:** Fitness function for direct transfer option on varying asteroid dimension

Considering that the Earth has a mean radius of about 6400 km and assuming that the NEO orbit at MOID passes through the center of the Earth, only the asteroid of 50 m can be deviated enough to miss the Earth. However, this is an extreme case. It is also important to remark that, if an higher deviation of the asteroid is required, the easy solution is to increment the mass of the impactor, because the linear momentum imparted to the NEO is directly proportional to the mass of the spacecraft [2].

Finally, it is interesting to notice that as the mass of the asteroid increases, the value of the fitness function tends to zero and the function tends to be flat; this behaviour can cause the genetic algorithm to converge to a sub-optimal solution, because there is small difference between two distinct set of decision variables. Therefore, when performing the optimisation for the largest asteroid, it is important to check the result with another optimisation where the mass of the NEO is decreased; in this way the fitness function varies more between two distinct individuals and this helps the convergence of the algorithm. This is valid for all the global optimisations performed.

#### 5.1.4.2 Direct transfer with DSM results

The second trajectory option increases the amount of decision variables from 2 to 6 and the spacecraft can perform a deep space manoeuvre to correct its orbit. The optimal values obtained for the decision variables are reported in Table 5.6.

| $\alpha$ [-] | $\beta$ [-] | TOF [days] | $\|\|\boldsymbol{\Delta V_0}\|\| \left[\frac{km}{s}\right]$ | $\psi_{\Delta V_0}[rad]$ | $\delta_{\Delta V_0}[rad]$ |
|---|---|---|---|---|---|
| 0.1211 | 0.9000 | 462 | 2.999 | 0.321 | -0.105 |

**Table 5.6:** Optimal decision variables for direct transfer with DSM

As for the direct transfer option, also in this case the solution is independent on the dimension of the NEO. The only points that change on the orbit depending on the asteroid dimension, are the position of spacecraft and asteroid at $t_{spot}$ (represented with the * sign), that is when the camera first see the NEO as a pixel. In Figure 5.5, it is possible to see the trajectory obtained; the coast phase before the manoeuvre is in red, then the trajectory becomes purple after the DSM.

At a first look, it is clear that the DSM manoeuvre happens at the last possible time, in fact the value of $\beta_{opt}$ coincides with its upper boundary. A similar result was obtained by Bolsi [2]. Moreover, the value of $\alpha_{opt}$ is very similar to the one obtained with the direct transfer option. In fact, by comparing Figure 5.4 and Figure 5.5, it is possible to see that are quite the same trajectory. This behaviour was not

expected but, considering that the ΔV of launch does not affect the mass of the spacecraft at impact, it is clearer why the algorithm converges to a solution where the ΔV to be given at the deep space manoeuvre point is small. In so doing, the solution spends the minimum amount of propellant at the DSM and the spacecraft preserves mass for the impact and therefore, the solutions for the direct transfer case and the transfer with DSM are very similar.

Regarding the ΔV at launch, also in this case the optimisation exploits all the energy that the launcher can provide; but, this time the $\boldsymbol{\Delta V_0}$ vector is less aligned with Earth's velocity, in fact the in-plane angle $\phi$ is about 20 degrees.

Analysing the ΔV given with the deep space manoeuvre, it is attested around 0.350 km/s and it is almost parallel to the velocity vector of the spacecraft; this manoeuvre adjusts the trajectory of the spacecraft to have an impact with the target even more parallel than in the case of the direct transfer. In fact the angle between velocity of the spacecraft and of the NEO is below 2 degrees. Moreover, the relative velocity spacecraft-NEO at impact is 19% higher than the one in the direct transfer case, reaching 2750 m/s.

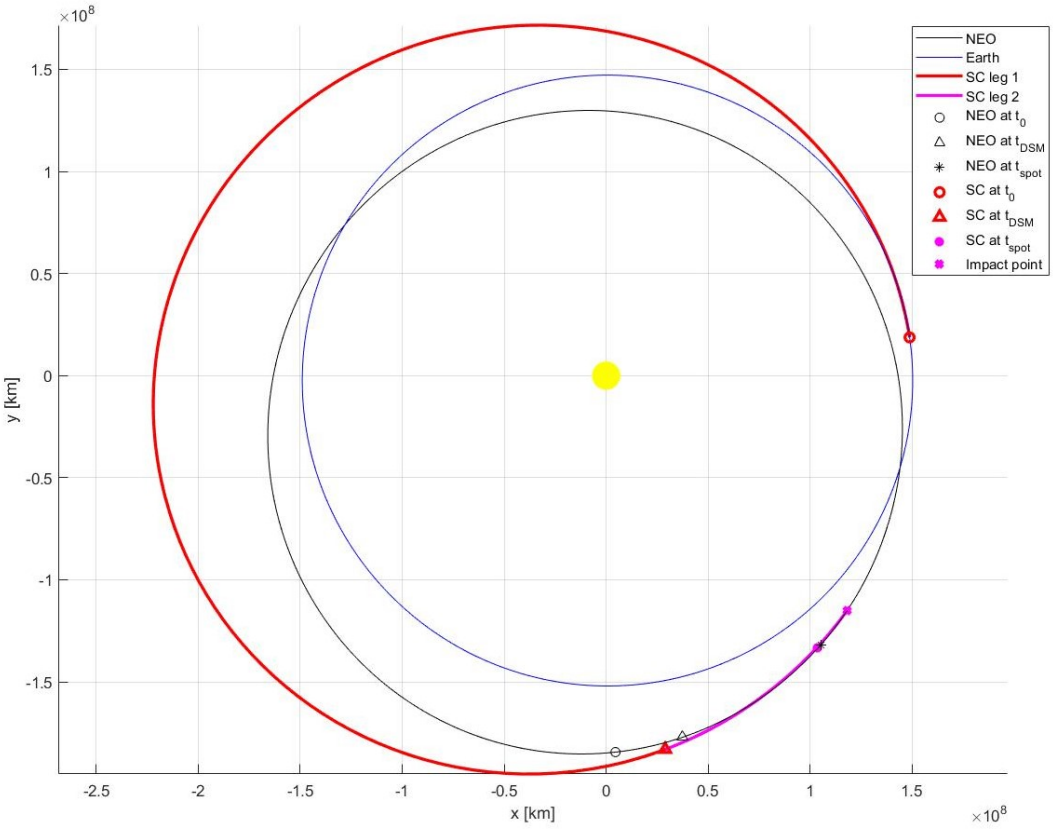


**Figure 5.5:** Direct transfer with DSM optimal trajectory

However, by comparing the values of the fitness function of this case reported in Table 5.7, with the direct transfer case without DSM, the solution is poorly improved of about 1%; for the biggest asteroid of 500 m in diameter the solution does not improve at all. This is due to the fact that, even if the velocity at impact is increased, the mass of the spacecraft is decreased because part of the propellant is burnt for the $\Delta V_{DSM}$. Hence, inserting a deep space manoeuvre seems not to improve so much the solution, this is why also the multi-revolution case is studied. Nevertheless, a planned DSM can be exploited to

correct errors in the orbit insertion of the spacecraft and also errors in the estimation of the the NEO's ephemerides.

| $D_{NEO}$ [m] | $J = -(r_p - r_{p_0})$ [km] |
|---|---|
| 50 | -10207 |
| 100 | -1219 |
| 200 | -151 |
| 500 | -10 |

**Table 5.7:** Fitness function for direct transfer with DSM option on varying asteroid dimension

#### 5.1.4.3 Multi-revolution transfer results

Moving to the optimisation of a multi-revolution transfer trajectory, the decision variables converge to the values in Table 5.8. In this case the value of $\alpha$ increases of about 0.1, meaning that the spacecraft departs from Earth in December 2088, almost two years after the direct transfer optimal trajectory. This can cause worst results in the fitness function with respect to the previous cases.

Also the time of flight is increased, because it is imposed that the spacecraft must perform an entire orbit before impact. This can be appreciate in Figure 5.6.

| $\alpha_{opt}$ [-] | $TOF_{opt}$ [days] |
|---|---|
| 0.2822 | 595 |

**Table 5.8:** Optimal decision variables for multi-revolution case

Also in this case, the spacecraft exploits the maximum ΔV provided by the launcher, and both the $\boldsymbol{\Delta V_0}$ vector and velocity of the spacecraft at impact are almost parallel (< 5 degrees) respectively to Earth's velocity at departure and asteroid's velocity at impact. In this case the relative velocity at impact is around 2500 m/s, at half way between the direct transfer trajectory and the one with the DSM.

Table 5.9 shows the deviation obtained with the different dimensions of the asteroid considered. In brackets are highlighted the difference in percentage with the results obtained with the direct transfer trajectory. Even if the velocity at impact is 10% higher than the one of the direct transfer case, the values of the optimised fitness function are the worst. As expected, this is mainly because the spacecraft departs from Earth two years later.

| $D_{NEO}$ | $J = -(r_p - r_{p_0})[km]$ |
|---|---|
| 50 | -8624 (-15%) |
| 100 | - 1035 (-14%) |
| 200 | - 128 (-15%) |
| 500 | - 8 (-20%) |

**Table 5.9:** Fitness function for multi-revolution transfer option on varying asteroid dimension.

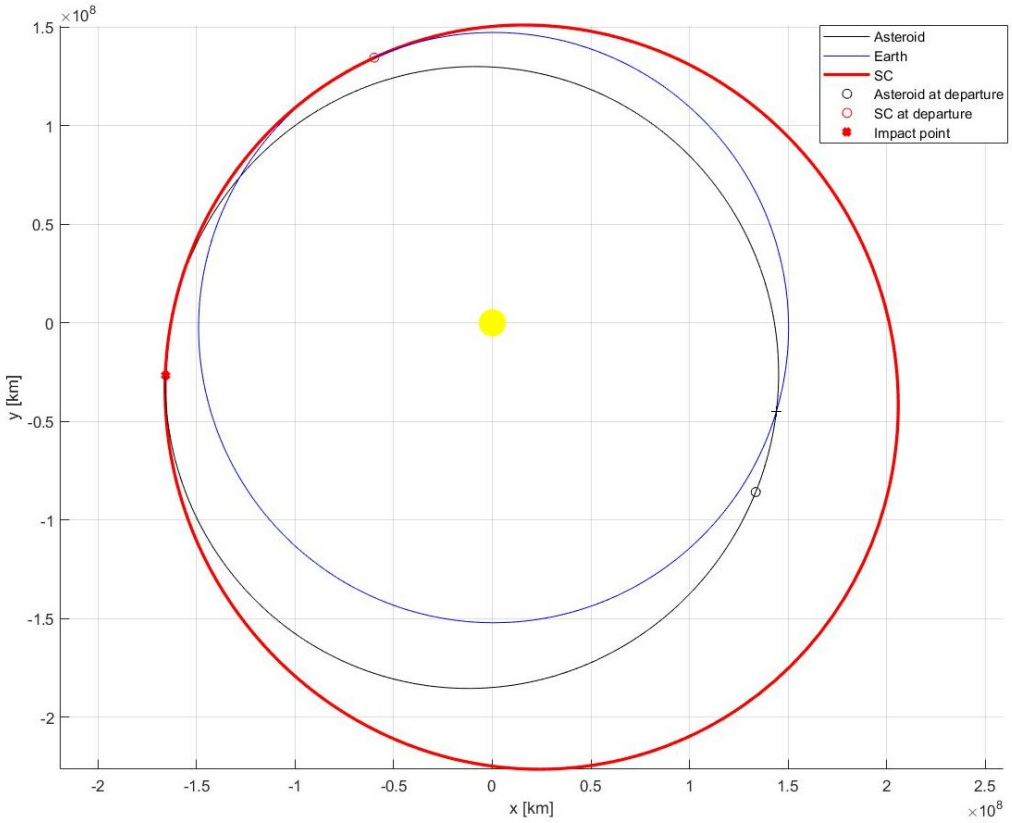


**Figure 5.6:** Multi-revolution transfer optimal trajectory

## 5.2 LOCAL OPTIMISATION

Once the nominal trajectory is computed with the global optimisation, it is time to refine this trajectory and add to the optimisation also the navigation phase to embed the GNC algorithm in the optimisation process. It is decided to add only at this point the real-time simulation because it is time consuming; in fact, a single run can vary from 1 minute up to 5 minutes. Since in the global optimisation, the number of fitness function evaluations is in the range of hundreds of thousands, it is not feasible to perform each time the simulation. For this optimisation, the multi-revolution case is discarded because it showed the lowest performance. The function used is fmincon because the aim is to refine the global solution.

In this section the considered case scenario is depicted; then, the new decision variables and the new fitness function to minimise are described. Finally, all the results obtained are reported and commented.

### 5.2.1 Case scenario

As case scenario, it is supposed that, when the spacecraft is at half of its trajectory, a new measurement of the orbital parameters of the NEO is available. Therefore, the spacecraft has to perform a deep space manoeuvre to correct its orbit based on the new information. In the case of the direct transfer, the DSM is performed as soon as the new measurement is available (at half the trajectory); instead, for the direct transfer with DSM the correction is forced to be at the same time the nominal DSM is planned.

However, for both cases some freedom is given to the algorithm to change when it performs the new manoeuvre. This is realized imposing a time window ($t_{window}$) of 20 days to perform the DSM, evenly split around the nominal manoeuvre point. The 20-day period is selected not to overturn the global solution.

For the generation of the new orbital parameters for the NEO, the NEODyS2 site citare collects the observations made on NEO and their ephemeris, MOID, the estimated orbital parameters and their 1-$\sigma$ variation. Therefore, the values of 1-$\sigma$ for the NEO 2010RF12 are taken as reference and are reported in Table 5.10.

These values are valid for the epoch 2020; however, they are taken as typical values of the uncertainty and are applied in the year 2085. The new orbit of the NEO is generated randomly taking the nominal Keplerian parameters as mean and considering a normal distribution with standard deviation equal to the 1-$\sigma$ variation of Table 5.10. In Table 5.10 are also reported randomly generated Keplerian parameters expect the true anomaly that does not describe the orbit. However, the true anomaly is randomly generated at spacecraft departure and it substitutes the nominal true anomaly of the NEO in that given moment. Since the spacecraft has already left Earth's orbit, it can correct its nominal trajectory only with a deep space manoeuvre.

| | 1-$\sigma$ variation | Random value |
|---|---|---|
| a [AU] | $3.924 \times 10^{-6}$ | 1.0559 |
| e [-] | $7.427 \times 10^{-6}$ | 0.1873 |
| i [deg] | $4.266 \times 10^{-4}$ | 0.9110 |
| $\Omega$ [deg] | $8.257 \times 10^{-4}$ | 162.8117 |
| $\omega$ [deg] | $1.838 \times 10^{-3}$ | 266.9983 |
| $\theta$ [deg] | $1.676 \times 10^{-2}$ | - |

**Table 5.10:** 1-$\sigma$ variation for 2010RF12 orbital parameters.

### 5.2.2 Optimisation variables and fitness function

Moving to the definitions of the decision variables, given that the spacecraft is already inserted in a trajectory only the time to perform the DSM and the time of flight are needed. Therefore, the decision variables are:

- $\beta$: defined as in section 5.1.2, it is a percentage from 0 to 0.9, used to compute the time to perform the DSM;
- $TOF_2$: is the time of flight from the deep space manoeuvre until impact and it is expressed in days.

The DSM time is computed with Eq. 5.5, exploiting the $TOF$ result of the global optimisation. Then, the impact conditions of the NEO are obtained propagating for $TOF_2$ days its motion from its position at $t_{DSM}$. The impact conditions of the spacecraft are obtained solving the Lambert problem between its position at $t_{DSM}$ and the position of the NEO at impact, imposing a time of flight equal to $TOF_2$.

Speaking of the acceptable values of the decision variables, it is decided that they can vary in the neighbourhood of the global optimisation results $\beta_{opt}$ and $TOF_{opt}$; the intention is not to alter too much the nominal optimised trajectory. For the direct transfer case, $\beta_{opt}$ is set to 0.5 so that the spacecraft will perform the manoeuvre around half the trajectory, that is the time at which the new measurement is available. The boundaries are computed exploiting $t_{window}$ as described in Table 5.11, where $TOF_{2_0} = (1-\beta_{opt})TOF_{opt}$ is the remaining time from the DSM until impact. The last constraint is the limit on the maximum ΔV the propulsion system can give to the spacecraft that is imposed as a non-linear constraint, like in section 5.1.2.

| | $\beta$ | $TOF_2$ |
|---|---|---|
| Boundaries | $\left[\beta_{opt} - \frac{1}{2}\frac{t_{window}}{TOF_{opt}} \quad \beta_{opt} + \frac{1}{2}\frac{t_{window}}{TOF_{opt}}\right]$ | $\left[TOF_{2_0} - \frac{t_{window}}{2} \quad TOF_{2_0} + \frac{t_{window}}{2}\right]$ |

**Table 5.11:** Boundaries for the decision variable of local optimisation

Regarding the optimisation process, the method used follows the flowchart in Figure 5.7. Once the genetic algorithm has returned the global optimal solution, the result is used to generate the first guess ($x_{2_0}$) for the fmincon algorithm. It is a vector of 2 decision variables equal to $[\beta_{opt} \quad TOF_{2_0}]$. After setting the bounds and constraint function, the minimisation of the objective function starts. At each step, the nominal trajectory adjusted for the updated NEO orbit is computed; at $t_{spot}$ the state of the spacecraft is randomly generated from the nominal values and the covariances reported in Section ref, and it is used as input for the simulation of the navigation phase. The simulation returns the estimated state of the spacecraft right before impact together with its covariance matrix. Assuming a normal distribution around the estimated spacecraft state with a standard deviation described by the covariance matrix, 1000 impact points are randomly generated, so that it is possible to compute the mean of the efficiencies $\mu_\epsilon$ and also the variance $\sigma_\epsilon$. In this way, the new objective function defined in Eq. 5.6 is obtained.

$$J_2 = -(\mu_\epsilon - 3\sigma_\epsilon) \; + \; w\,\Delta V_{DSM} \tag{5.6}$$

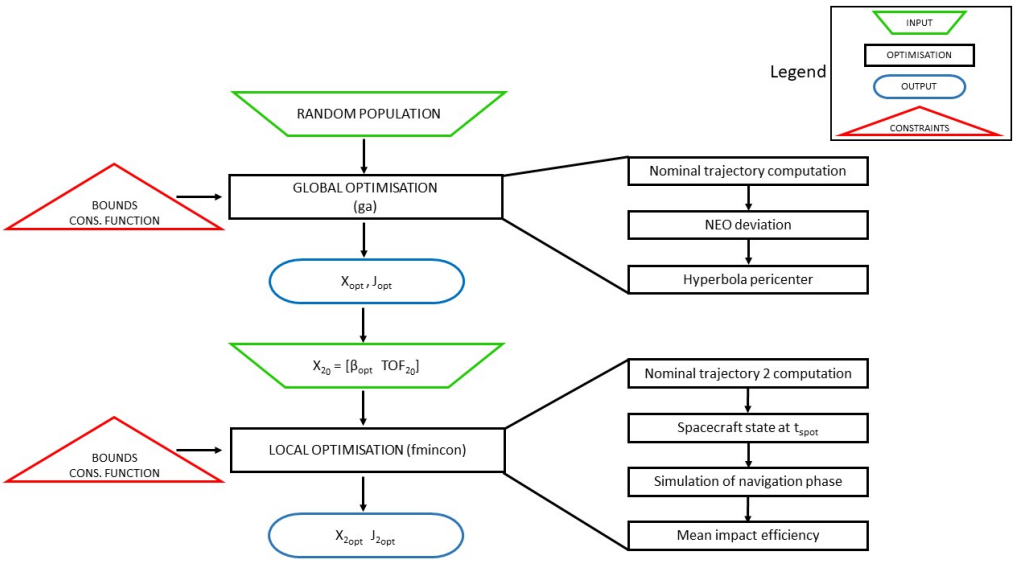


**Figure 5.7:** Flowchart of the optimisation process.

It is decided to generate 1000 points and optimise the mean of the efficiencies, in order to perform a robust optimisation following the article [38]. In a robust optimisation, N randomly generated solutions are chosen in a neighborhood of a solution x; for each solution is computed its objective function and the mean is used as real objective function by the optimiser. This causes N more function evaluations than a classical optimisation, but the solution obtained is robust.

In this thesis, the generation of 1000 distinct solutions around the neighborhood of a solution $x$ is not feasible, because will mean to simulate the navigation phase 1000 times for each iteration of the optimisation algorithm and this is too time consuming. Therefore, it is decided to exploit the availability of the covariance matrix to generate the 1000 points after the simulation. This approach does not precisely follow the procedure of [38], but taking 1000 close solutions and computing for every solution one efficiency, would obtain results similar to this alternative method. Moreover, with this approach, the problem of selecting a justifiable dimension of the neighborhood is avoided, because all the information is stored in the covariance matrix.

Returning to the definition of the objective function other terms appear; one is the variance $\sigma_\epsilon$, and it is subtracted in order to minimise the mean of the efficiencies with a confidence level of $3\sigma$. The other term is the norm of the $\Delta$V spent to perform the deep space manoeuvre; it is also multiplied by a weight, $w$, that has value 0.1 in order to have the efficiency term and the $\Delta$V term with a similar absolute value.

The $\Delta V_{DSM}$ term is essential, because the efficiency of impact does not depend on the mass of the spacecraft, since it is obtained comparing the nominal momentum transfer and the simulated one, both computed with the mass of the spacecraft after the DSM; therefore, optimising only the efficiency, converges to solutions where the spacecraft uses all the propellant for the deep space manoeuvre, leaving nothing for the navigation phase.

### 5.2.3 Local optimisation results with varying NEO dimension

In this section the local optimisation results for both the direct transfer trajectory and the direct transfer with pre-planned DSM trajectory with varying asteroid dimension are reported. The two cases are analysed together and the results are visible in the Tables 5.12 and 5.13.

| $D_{NEO}[m]$ | $\beta_2$ [-] | $TOF_2$ [days] | $\mu_\epsilon$ [-] | $\sigma_\epsilon$ [-] | $\Delta V_{DSM}$ [km/s] |
|---|---|---|---|---|---|
| 50 | 0.5000 | 231 | 0.0350 | 0.0201 | 0.176 |
| 100 | 0.5004 | 232 | 0.1297 | 0.0616 | 0.177 |
| 200 | 0.5000 | 230 | 0.3725 | 0.1079 | 0.177 |
| 500 | 0.4950 | 231 | 0.7871 | 0.0214 | 0.154 |

**Table 5.12:** Decision variables and fitness function for direct transfer local optimisation.

By comparing the amount of $\Delta$V spent for the deep space manoeuvre, it is higher for the case with pre-planned DSM with respect to the direct transfer case. This is easily explained by the fact that in the direct transfer case the DSM is performed at half the trajectory, 230 days before impact; instead for the pre-planned DSM case the burn is performed 45 days before impact. Therefore, it is more efficient to correct the spacecraft trajectory as soon as new estimation of the NEO orbital parameters are obtained. Figure 5.12 shows the trajectory obtained with the local optimisation of the direct transfer case, where it is possible to appreciate the point in which the DSM is performed.

| $D_{NEO}[m]$ | $\beta_2$ [-] | $TOF_2$ [days] | $\mu_\epsilon$ [-] | $\sigma_\epsilon$ [-] | $\Delta V_{DSM}$ [km/s] |
|---|---|---|---|---|---|
| 50 | 0.8975 | 45 | 0.0347 | 0.0194 | 0.792 |
| 100 | 0.9000 | 45 | 0.1322 | 0.0624 | 0.854 |
| 200 | 0.8989 | 46 | 0.3741 | 0.1054 | 0.833 |
| 500 | 0.9000 | 46 | 0.7837 | 0.0202 | 0.918 |

**Table 5.13:** Decision variables and fitness function for direct transfer with pre-planned DSM local optimisation.

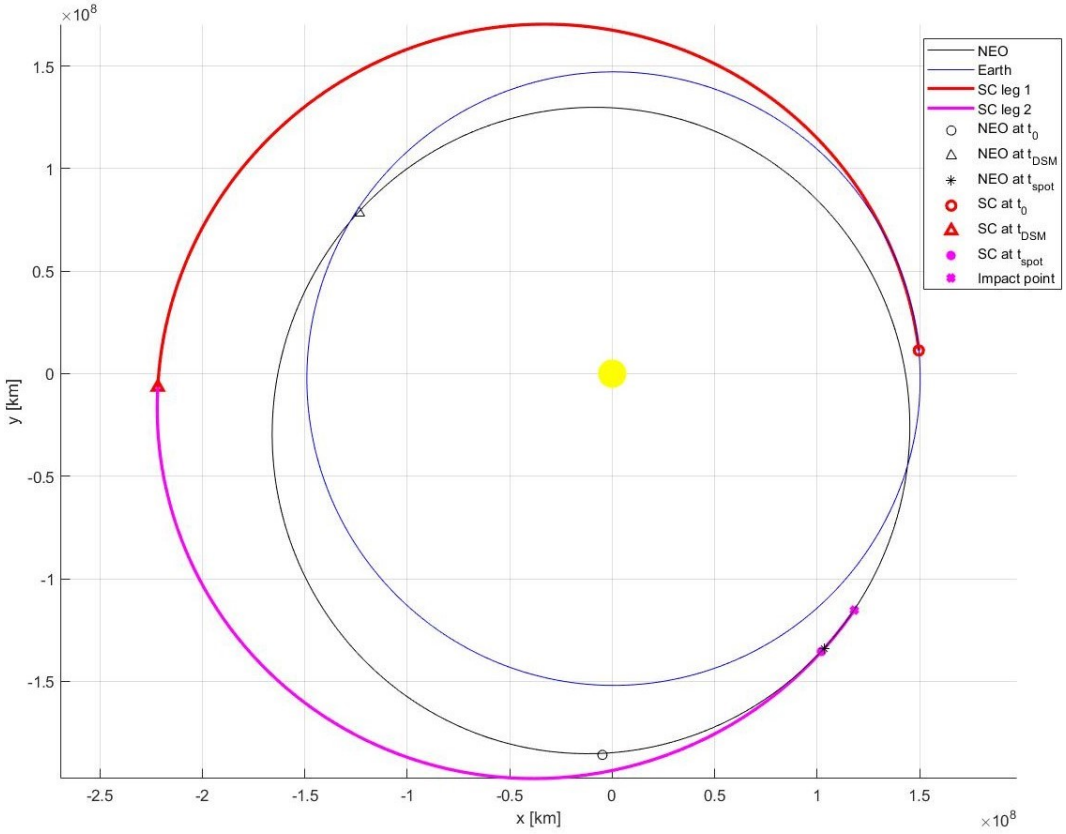


**Figure 5.8:** Direct transfer case after local optimisation.

Analysing instead the values that $\beta$ assumes and recalling that the nominal value of $\beta$ for the direct transfer case is 0.5, it can be seen that in some cases the solution does not change. Only in the optimisation of the trajectory impacting the asteroid of 500 m in Table 5.12, the value of $\beta$ decreases of 0.005; this, corresponds to anticipate the DSM of 2.3 days and also the impact time is decreased of that amount of time. Performing earlier the DSM, allows the spacecraft to save 20 m/s of $\Delta$V, that corresponds to 4 kg of propellant. Also for the pre-planned DSM case the solutions with lower $\beta$ saves propellant performing the manoeuvre slightly before.

However, these improvements are totally negligible. What it is possible to say is that, once the spacecraft is inserted on an optimised nominal trajectory, this kind of optimisation does not change the solution. This because the efficiency of impact depends more on the control algorithm applied during the navigation and on the sensors installed on the spacecraft. Therefore, the values of fitness function are flat in the region considered causing the fmincon algorithm to, in some cases, retain the

starting point of the optimisation as the optimal solution.

What can be interesting to analyse, is the tendency of the efficiency of impact as the dimension of the NEO decreases. As it is for the probability of impact, the bigger the asteroid the better is the efficiency. The efficiency goes from 78% for 500 m diameter asteroid to 37% for the 200 m, 13% for 100 m and only 3.5 % for 50 m asteroid.

The drop of efficiency for the 200 m asteroid is understood by plotting the typical distribution of the impact points obtained from the simulations. Comparing Figure 5.11 with Figure 5.12, that represents the impact points for the biggest asteroid, it is possible to appreciate how in the last Figure the impact points are more concentrated than in the first one; this leads to an higher efficiency for most points because the impact angle is low and also the variance of the efficiency is contained. On the other hand, for the 200 m asteroid, even if the probability of hitting the asteroid is about 70%, the impact points are more spread on the surface leading to a worse efficiency and variance as it is possible to see from Table 5.12 and 5.13. Instead, the variance for the 100 m and 50 m asteroid is lower, because the probability of impact is respectively 30% and 8%; this means that in the majority of the runs the spacecraft can not even impact the asteroid as shown in Figure 5.9 and 5.10, where the number of blue dots is significantly less than the 200 and 500 m asteroids figures. All these cases that do not hit the asteroid have zero efficiency and this translates into a low variance of the efficiencies.

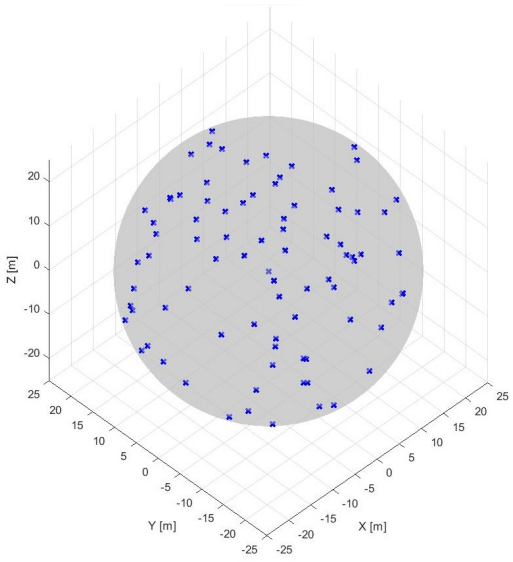


**Figure 5.9:** Impact points for 50 m asteroid.

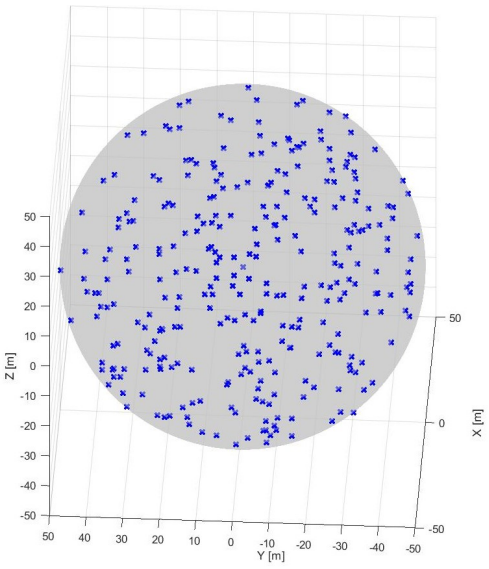


**Figure 5.10:** Impact points for 100 m asteroid.

Considering the behaviour of the control algorithm, even if the initial time of the simulation is 60 days before impact, like for the 500 m asteroid case, the control action starts between 1 and 0.5 days before impact. This is because the control action is enable only when a good estimation of the position of the target is obtained; Figure 5.13 illustrates the covariances of the estimated lateral position of the spacecraft with respect to the NEO, that correspond to the Zero Effort Miss; while, in red is highlighted the maximum values of the covariances acceptable to activate the thrusters. As it can be seen, only in the last part of the navigation, the curves of the covariances go under the limit and the control action is enabled. At the beginning of navigation, these curves increase because the covariance depends on the estimated distance from the target and the initial value set for the covariances is decided a priori without taking into account the distance; as the time pass and the spacecraft approaches the asteroid, the values decrease.

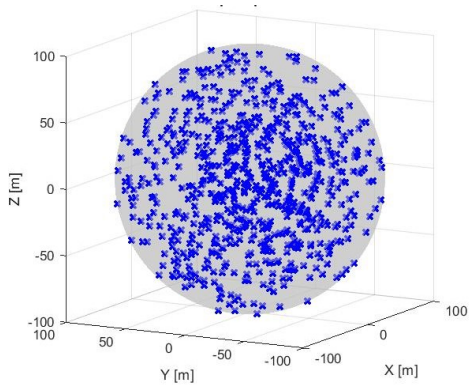


**Figure 5.11:** Impact points for 200 m asteroid.

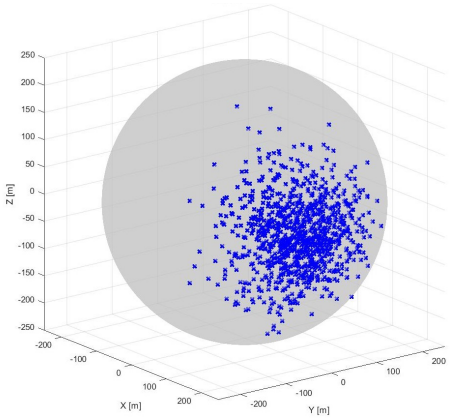


**Figure 5.12:** Impact points for 500 m asteroid.

Starting the control action from this far, causes the spacecraft to use an amount of $\Delta V$ below 200 m/s, that translates in 30 kg of propellant burnt by the thrusters. It was tried to perform simulations increasing the limit to enable the control to see if give more time to control the spacecraft can improve the results. Even small changes can cause additional days of control action; for example, increasing the limit value of the covariance to 3.1 doubles the control time, obtaining in the case of the 500 m asteroid a control time of approximately 1 day. This solution increases the computational time, because the algorithm has to compute the thrust of the actuators for more integration steps, but it does not improve the efficiency of impact.

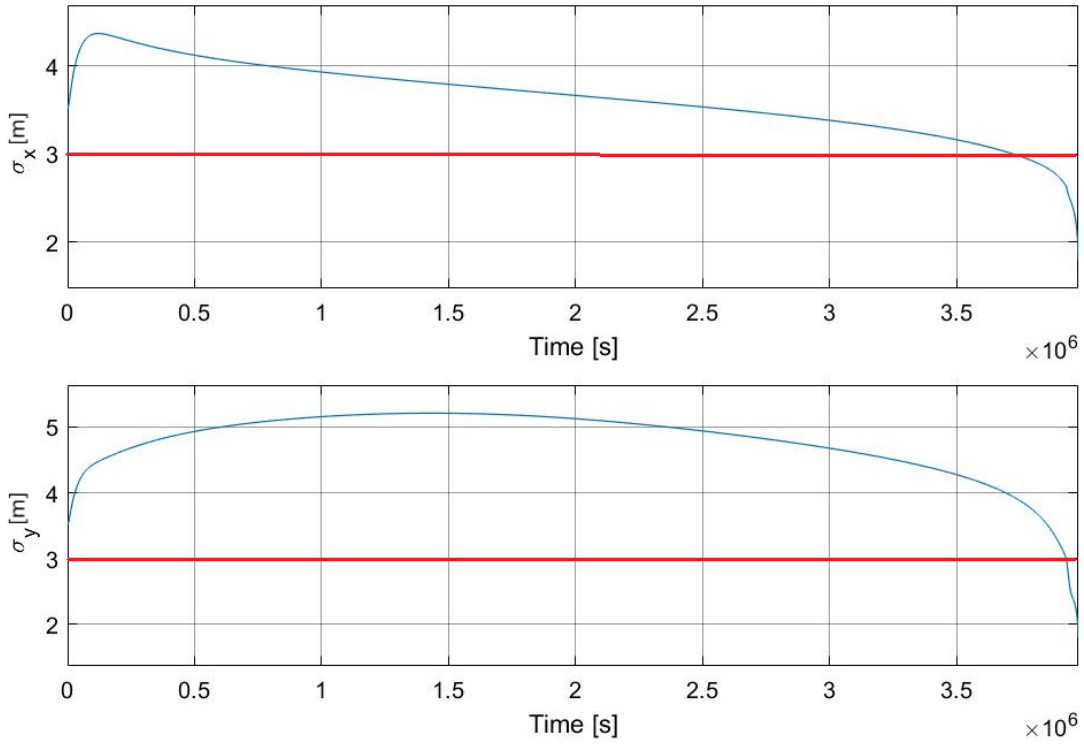


**Figure 5.13:** Covariance of estimated lateral position of the spacecraft with respect to the target

# 6 Conclusions

The goal of this work was to create a tool that can be adapted to different asteroid's dimension, shape and orbit and that can optimise an entire mission simulating the approach of the spacecraft towards a target NEO and computing the efficiency of the impact obtained.

The optimisation of the nominal trajectory has obtained good results, comparable with the ones of other studies; instead, regarding the local optimisation of the trajectory, the results obtained are less satisfying because in most cases the solution does not change significantly. However, the capability of performing a robust optimisation of the trajectory has been demonstrated, Moreover, this approach can be suited when a 3D model of a possible target is available, so that the results obtained will be even more reliable. In any case, other tests with other targets are necessary to validate this approach.

Overall, a simple tool has been created, that from the output of a simulation can compute the efficiency of the impact. Considering the efficiencies obtained, the control algorithm tested can hit an asteroid of 500 meters 100% of the time with an efficiency higher than 70%. Its performance decreases too much when it tries to impact asteroid smaller than 200 meters. d

## 6.1 FUTURE WORKS

Here, a list of possible future improvements of this study is presented.

### 6.1.1 Different optimisation

The first suggestion is to try this tool with other possible threat asteroids and comparing them with the results of this work. It is also suggested to think of other fitness functions that can exploit the results of the navigation phase to improve the overall trajectory; one possibility can be easily the probability of impact with the asteroid.

### 6.1.2 Different control algorithm

Another improvement can be achieved by tuning the control algorithm. It can be interesting to see what happens if the thrust-to-weight ratio is increased, amplifying in this way the control action and the capability to correct in less time the same positioning error. Then, it can be interesting to see also if an increment in the acquisition rate of the camera can increase the efficiency ad probability of impact for the smaller asteroids. On the other hand, this choice will increase the computation time.

Finally, it is possible to try new control algorithms. For example, algorithms that fire the thrusters at discrete times. Moreover, since in this work the navigation time is extended a lot with respect to the previous work on this subject, a control algorithm with variable acquisition rate of the camera could be more suited, instead of a constant acquisition rate.

### 6.1.3 Other impact models and asteroids

Concerning the impact model, other types of empirical formulations are present, for example some that rely on the knowledge of the porosity of the asteroid. Others, can also estimate the crater that the impact generates. So, this part can be further amplified to distinguish between asteroids of different classes.

It is also important to see what happens when the shape of the asteroid is ellipsoidal instead of spherical. But before doing so, it is suggested to improve the image analysis because with elliptic shapes the results obtained are worse.

### 6.1.4 Impact detection with 3D model

If the asteroid has a regular shape, the approximation with an ellipsoid can be acceptable. But, when the shape of the asteroid is very complex, it could be more correct to use directly the 3D model of the asteroid. This requires the integration in time of the last moments before impact and increases the computation time, but it is workable.
Moreover, using directly the 3D model can count for the asperity of the surface of the asteroid that can cause a variation of the impact efficiency.

### 6.1.5 Ray tracing

The last idea is to generate the image of the asteroid via ray tracing. Till now blender is not using the ray tracing, but this option can be turned on; this will increase a lot the computation effort. Moreover, it is also possible to compute the ray tracing directly with Simulink, that has already built-in models available. This would cut off from the simulation the software Blender, saving computational time.

# Bibliography


[1] Giovanni Purpura, *Development and simulation of an autonomous navigation and control strategy for an asteroid impactor mission*, 2018,„ Politecnico di Milano, Faculty of Industrial Engineering, Department of Aerospace Science and Technologies, Master in Space Engineering, Advisor: Pierluigi Di Lizia.

[2] Lorenzo Bolsi, *Optimal Deflection Of Near-Earth Objects Through a Kinetic Impactor Performing Gravity Assist*, 2018, Politecnico di Milano, Faculty of Industrial Engineering, Department of Aerospace Science and Technologies, Master in Space Engineering, Advisor: Camilla Colombo.

[3] Mathieu Petit, *Optimal Deflection of Resonant Near-Earth Objects using the B-Plane*, 2018, Politecnico di Milano, Faculty of Industrial Engineering, Department of Aerospace Science and Technologies, Master in Space Engineering, Advisor: Camilla Colombo.

[4] Camilla Colombo, Massimiliano Vasile, Gianmarco Radice *Semi-Analytical Solution for the Optimal Low-Thrust deflection of Near-Earth Objetcs*, 2009.

[5] C. Colombo a, M. Albano b, R. Bertacin et al., *Mission analysis for two potential asteroids threat scenarios: optimal impact strategies*, 2017.

[6] Joan Pau Sanchez Cuartielles, Camilla Colombo, Massimiliano Vasile et al., *A Multi-criteria Assessment of deflection Methods for Dangerous NEOs*, 2007.

[7] J. P. Sanchez, C. Colombo, *Impact Hazard Protection Efficiency by a Small Kinetic Impactor*, 2013.

[8] Massimiliano Vasile, Camilla Colombo, *Optimal Impact Strategies for Asteroid Deflections*, 2008.

[9] Massimo Vetrisano, Camilla Colombo, Massimiliano Vasile, *Asteroid rotation and orbit control via laser ablation*, 2015.

[10] 2019 IAA Planetary Defense Conference, *Conference Summary and Recommendations*, 2019.

[11] V. V. Shuvalov, V. V. Svettsov, I. A. Trubetskaya, *An Estimate for the Size of the Area of Damage on the Earth's Surface after Impacts of 10–300 m Asteroids*, 2013.

[12] ESA, *Risky asteroids*, 2020. `https://www.esa.int/Safety_Security/Risky_asteroids`.

[13] 2020. ESA. *Near-Earth Object Coordination Centre*. `https://www.esa.int/Safety_Security/Near-Earth_Object_Coordination_Centre`.

[14] Tricia Talbert, *Near-Earth Object Observation Program*, 2019. `https://www.nasa.gov/planetarydefense/neoo`.

[15] CNEOS, *NEO Basics*, 2020. `https://cneos.jpl.nasa.gov/about/neo_groups.html`

[16] Michael C. Nolan, *NASA 3D Resources*, 2016. `https://nasa3d.arc.nasa.gov/detail/bennu`

[17] ESA, *NEODyS-2 Near Earth Objects - Dynamic Site*, 2020. `https://newton.spacedys.com/neodys/index.php?pc=1.1.0&n=2010RF12`

[18] Steven R. Chesley, Paul W. Chodas, Andrea Milani et al., *Quantifying the Risk Posed by Potential Earth Impacts*, 2001.

[19] Ian Carnelli, Andrés Gàlvez, Dario Izzo, *Don Quijote: A NEO Deflection Precursor MissionDON QUIJOTE*, 2006.

[20] Patrick Michel, Michael Kueppers, Holger SIerks et al., *European component of the AIDA mission to a binary asteroid: Characterization and interpretation of the impact of the DART impactor*, 2017.

[21] Hayabusa2 Project Team, *Hayabusa2 Information Fact Sheet*, 2018.

[22] Jun'ichiro Kawaguchi, Akira Fujiwara and Tono Uesugi, *Hayabusa—Its technology and science accomplishment summary and Hayabusa-2*, 2008.

[23] D.S. Lauretta, S.S. Balram-Knutson, E. Beshore et al., *OSIRIS-REx: Sample Return from Asteroid (101955) Bennu*, 2017.

[24] A. W. Harris, L. Drube, L. Johnson, *Roadmap of Relevant Research for Planetary Defense*, 2017.

[25] A. F. Cheng, P. Michel, M. Jutzi et al., *Asteroid Impact & Deflection Assessment mission: Kinetic impactor*, 2016.

[26] Report to Congress, *Near-Earth Object Survey and Deflection Analysis of Alternatives*, 2007.

[27] Alessandro A. Quarta, Giovanni Mengali, *Electric sail missions to potentially hazardous asteroids*, 2009.

[28] Masahisa Yanagisawa, Sunao Hasegawa, Nobutoshi Shirogane, *Momentum and Angular Momentum Transfer in Oblique Impacts: Implications for Asteroid Rotations*, 1993.

[29] Masahisa Yanagisawa, Sunao Hasegawa, *Momentum Transfer in Oblique Impacts: Implications for Asteroid Rotations*, 1999.

[30] Fei Zhang, Bo Xu, Christian Circi et al., *Rotational and translational considerations in kinetic impact deflection of potentially hazardous asteroids*, 2017.

[31] D.J. Scheeres, R.L. Schweickart, *The Mechanics of Moving Asteroids*, 2004.

[32] A.F. Cheng, H.A. Weaver, S.J. Conard, *Long-Range Reconnaissance Imager on New Horizons*, 2007.

[33] Justin A. Atchison, Mark A. Jensenius, Michelle H.Chen et al., *Double Asteroid Redirection Test-Mission Design and Navigation*, 2013.

[34] Justin A. Atchisonn, Martin T. Ozimek, Brian L. Kant, *Trajectory options for the DART mission*, 2016.

[35] D. L. Hampton, J. W. Baer, M. A. Huisjen et al., *An overview of the instrument suite for the Deep Impact mission*, 2004.

[36] X. Ma, J. Fang and X. Ning, *An overview of the autonomous navigation for a gravity-assist interplanetary spacecraft*, 2013.

[37] B. D. Tapley, B. E. Schutz and G. H. Born, *Statistical Orbit Determination*, 2004.

[38] Kalyanmoy Deb,Himanshu Gupta, *Introducing Robustness in Multi-Objective Optimization*, MIT 2006.

[39] MathWorks, *Global Optimisation Toolbox User's Guide*, Version 4.1, March 2019 `https://it.mathworks.com/help/pdf_doc/gads/index.html`.

[40] H. Shen, P. Tsiotra, *USING BATTIN'S METHOD TO OBTAIN MULTIPLE-REVOLUTION LAMBERT'S SOLUTIONS*, 2003.

[41] Ebisuzaki, Toshikazu, Quinn et al., *Demonstration designs for the remediation of space debris from the International Space Station*, 2015.

[42] Wenwen Zhang, Qian Chen, *Signal-to-Noise Ratio Performance Comparison of Electron Multiplying CCD and Intensified CCD Detectors*, 2009.

[43] Hamamatsu datasheet, *CCD area image sensor S12101*, 2017. `https://www.hamamatsu.com/resources/pdf/ssd/s12101_kmpd1176e.pdf`